Wave-packet dynamics in multilayer phosphorene

S. M. Cunha,[*] D. R. da Costa,[†] G. O. de Sousa,[‡] Andrey Chaves,[§] J. Milton Pereira, Jr.,[‖] and G. A. Farias[¶]
Departamento de Física, Universidade Federal do Ceará, Caixa Postal 6030, Campus do Pici, 60455-900 Fortaleza, Ceará, Brazil

(Received 26 March 2019; published 21 June 2019)

We investigate the dynamics of Gaussian wave packets in multilayer black phosphorus (BP). Time-dependent average position and velocity are calculated analytically and numerically by using a continuum model and a method based on the split-operator technique, respectively. By analyzing the wave-packet trajectories with nonvanishing initial momentum along y direction, we observed transient spatial oscillations due to the effect known as zitterbewegung (ZBW). We also demonstrated, based on the Heisenberg picture and by the calculation of the velocity operators, that the trembling motion along the y direction at small times is unavoidable even for null initial momentum. We verified that the ZBW is directly related to the splitting of the wave packet into two parts moving with opposite velocities, as similar to graphene, and the linear dependence on k_y in out-of-diagonal terms in the Hamiltonian. In addition for phosphorene systems, the two portions of the propagated wave packets have an asymmetric shape for unbalanced ($[1, 0]^T$) and phased different ($[1, i]^T$) initial pseudospin components, playing an important role in the amplitude, frequency and duration time of the transient oscillations. Electrons in the vicinity of the Fermi energy traveling in N-layer phosphorene also exhibit qualitatively similar trembling motion and transient character as found in the monolayer case, except by the oscillation phase difference and final group velocity achieved after the transient behavior. As a consequence of the anisotropy on the N-layer BP energy bands, effective masses and group velocities along the x and y directions, the wave packet propagates nonuniformly along the different directions and deforms into an elliptical shape. By comparing our analytical results with those ones obtained by the split-operator technique, we verified a good qualitative and quantitative agreement between them, except for very larger values of wave vector and after long time steps.

DOI: 10.1103/PhysRevB.99.235424

I. INTRODUCTION

The well-known zitterbewegung (ZBW) phenomenon, a trembling motion caused by interference between positive and negative energy states [1,2], was predicted by Schrödinger in 1930 for the motion of relativistic electrons in vacuum governed by the Dirac equation and has been subject of renewed interest over the past decade in various condensed matter systems [3,4]. This oscillatory dynamic of the center of a free wave packet is manifested in the time evolution of the expectation values of some physical observables, such as position, velocity, current, and spin angular momentum. The characteristic frequency of ZBW motion is determined by the gap between the two states with positive and negative energies and is of the order of $2m_0c^2/\hbar$, where m_0 is the bare electron mass, c is the speed of light, and $\hbar$ is the Planck constant, whereas the amplitude of oscillations is of the order of the Compton wavelength, i.e., $\hbar/m_0c$. This corresponds to large oscillation frequencies of $\approx 10^{21}$ Hz and small oscillation amplitudes of $\approx 10^{-3}$ Å, making its direct experimental observation a really hard task [4–10]. Although, the ZBW is, in principle, a relativistic effect, it may arise even for a nonrelativistic particle moving in crystalline solids if their band structures could be represented by a two-band model reminiscent of the Dirac equation [11–13], or for quasiparticles governed by the Bogoliubov-de Gennes equations in superconductors [14,15], in which the energy-wave-vector dependence is similar to the relativistic relation, or in some semiconductor nanostructures with spin-orbit coupling [15–22].

Two of the pioneering works investigating the ZBW effect in narrow-gap semiconductors are the theoretical studies of Schliemann [16] and Zawadzki [23] in 2005, which considered the coupling between the positive-negative energy eigenstates of the quantum systems using a two energy bands model. Zawadzki [23] demonstrated that semiconductor electrons experience a ZBW, considering the analogy between the band structure of narrow-gap semiconductors and the Dirac equation for relativistic electrons in vacuum. The former exhibits more experimentally favorable frequency and amplitude characteristics than electrons in a vacuum. Schliemann *et al.* [16,17] studied the ZBW of electronic wave packets in III-V zinc-blende semiconductor quantum wells in the presence of spin-orbit coupling of the Rashba and Dresselhaus type, by using the Hamiltonian of spin splitting (the Bychkov-Rashba mechanism), which requires structure inversion asymmetry of the system. These works triggered a strong interest in the theoretical investigations of wave-packet dynamics and ZBW oscillations in other physical systems, as, for instance, 2D photonic crystal [24,25], 2D sonic crystal [26], trapped ion [27,28], hole Luttinger systems [29,30], ultracold atoms

[*]sofiacunha@fisica.ufc.br
[†]diego_rabelo@fisica.ufc.br
[‡]gabrieloliveira@fisica.ufc.br
[§]andrey@fisica.ufc.br
[‖]pereira@fisica.ufc.br
[¶]gil@fisica.ufc.br

[31,32], topological insulators [33,34], and electromagnetic pulses propagating through metamaterials presenting an optical analog ZBW effect [35]. Experimental observations of ZB phenomenon have been reported in 2008 for macroscopic sonic crystals [26], in 2010 for trapped ion systems [27] and for photonic superlattices [25], and in 2013 for spin-orbit-coupled Bose-Einstein condensates [36,37].

In the last two decades, the production of graphene has led to a significant level of interest on the physics of layered materials [38–41]. This interest is not only due to its possible future technological applications, but also because it provides the possibility to probe interesting phenomena predicted by quantum field theories not found in conventional semiconductors and metals. One of these exotic properties of low-energy electrons in single- and few-layer graphene, described by the zero mass Dirac equation, is the existence of ZBW as reported in Refs. [42–52] for monolayer and [42,46,53] bilayer graphene. Maksimova *et al.* [43] in 2008 analyzed the detailed description of wave-packet evolution in monolayer graphene, using the Green's function representation and the low-energy Dirac equation, and investigated the influence on the wave-packet dynamics of different pseudospin polarizations for the initial wave function and the phenomenon of ZBW of the packet center. Similar investigation was performed numerically by Chaves *et al.* [54] in 2010 by means the split-operator technique. Rusin and Zawadzki [46] studied the evolution of the wave packet in bilayer graphene and found the analytical expressions for the pseudospin components of wave function and average position operator as well as analytical results for the ZBW oscillations. They demonstrated that the transient character ZBW in bilayer graphene is related to the increasing spatial separation of the subpackets corresponding to the positive and negative energy states moving in opposite directions, in a similar way to some pseudospin configurations in monolayer graphene, and not only due to the packet's slow spreading which in turn is responsible for the attenuation and decay of ZBW.

Most recently, there is growing interests in black phosphorus (BP), also known as phosphorene [55–60]. It is a semiconductor with puckered structure due to its sp^3 hybridization and displays a tunable band gap [55,56,59,61–71] ranging of 1.8 eV for single-layer BP to ≈0.4 eV for bulk samples, which is very relevant for possible technological applications [55,56,72–76]. BP presents a highly anisotropic band structure and consequently a large anisotropic effective mass [69]. Although previous works have studied wave-packet propagation for standard semiconductors [1,2,16,17,21–23], monolayer [42–52] and bilayer [42,46,53] graphene, silicene,[77] and transition metal dichalcogenide [78], no similar theoretical investigation on wave-packet propagation in N-layer BP system was reported in the literature, to the best of our knowledge. Therefore it is also interesting to see whether the results observed in these cited 2D materials differ or are similar for multilayer phosphorene, and if the anisotropic character of electronic properties of multilayer phosphorene implies in any atypical feature in the dynamics of the wave packets.

The paper is organized as follows. In Sec. II, we present the theoretical models used to describe the time evolution of wave packets in multilayer phosphorene systems, based on (Sec. II A) the continuum approximation [69,79,80] for low-energy electrons. The two frameworks are depicted in Secs. II B and II C), described within the Green's function formalism and the split-operator technique [54,81–93] for the expansion of the time-evolution operator, respectively. In Sec. III, the analytical expressions for some physical quantities, such as the average values of position operator and the components of wave function, are found for different configuration of initial pseudospin polarization and these results are compared with the numerical split-operator ones in order to check the limit of accuracy of the both models. We also show the probability amplitudes of the wave packet at different time steps ($t > 0$) to understand the origin of transient character of the oscillations on the average positions. An important remark concerning the wave-packet dynamics is about the oscillatory behavior of the velocity as a manifestation of zitterbewegung on the wave-packet motion. Therefore, in Sec. IV, we calculate the velocity operators and their commutators with the continuum Hamiltonian for multilayer phosphorene in order to verify whether v_x and v_y are constants of motion or not, and thus check the consistency of our formalism. Concluding remarks are reported in Sec. V.

II. THEORETICAL MODEL

In this section, we present the theoretical frameworks used to obtain the physical observables of a Gaussian wave packet moving along a N-layer BP system discussed in the following sections by assuming an arbitrary initial pseudospin polarization. In both formalisms described in Secs. II B and II C, we use the continuum model discussed in Sec. II A.

A. Continuum approximation for N-layer phosphorene and the polarization angle

Based on the tight-binding model for multilayer phosphorene reported by Rudenko *et al.* [94] involving ten intralayer and four interlayer hopping parameters and with the layers alignments obeying the AB stacking [see Fig. 1(a)], a simple analytical model was recently derived within the long-wavelength approximation to describe low-energy charge carriers in N-layer BP sheet around Γ point [69]. In this continuum approximation, the Hamiltonian for the N-layer BP is composed by N blocks of 2×2 monolayer-type BP Hamiltonians where each one of these effective monolayer Hamiltonians is formed by layer-dependent Hamiltonian coefficients and reads in momentum space as

$$\mathcal{H} = \begin{pmatrix} u_0^n + \eta_x^n k_x^2 + \eta_y^n k_y^2 & \delta^n + \gamma_x^n k_x^2 + \gamma_y^n k_y^2 + i\chi^n k_y \\ \delta^n + \gamma_x^n k_x^2 + \gamma_y^n k_y^2 - i\chi^n k_y & u_0^n + \eta_x^n k_x^2 + \eta_y^n k_y^2 \end{pmatrix}, \quad (1)$$

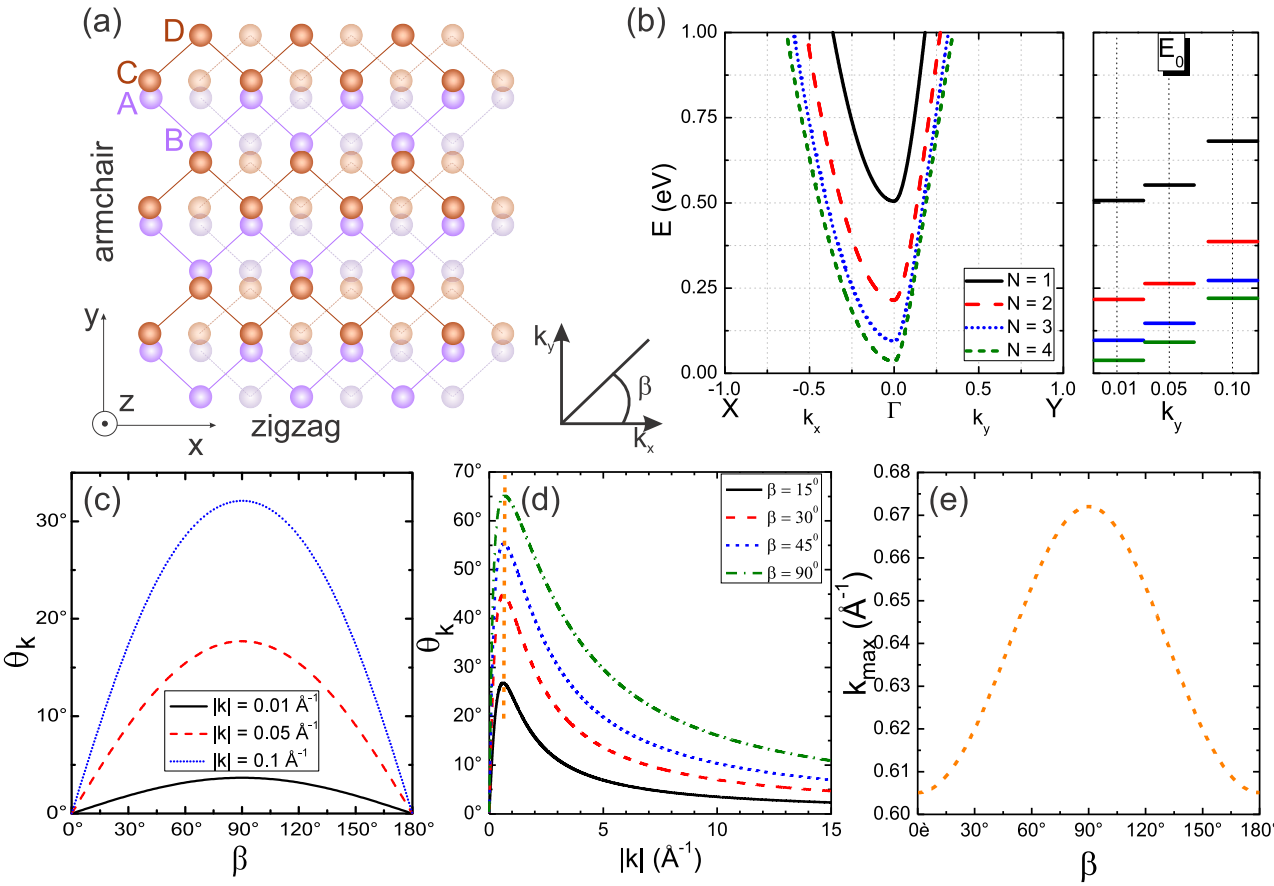

FIG. 1. (a) Top view of lattice structure of AB-stacked N-layer BP system, emphasizing the orientations of the lattice adopted in this work and the four sublattices: A and B at bottom sublayer (purple symbols), and C and D at top sublayer (brown symbols). The x and y coordinates correspond to the zigzag and armchair directions, respectively, and z direction is the out-of-plane direction. (b) (Left) Lowest electronic energy band obtained by diagonalizing the Hamiltonian (1) with $n = N$ for monolayer (black solid curve), bilayer (red dashed curve), trilayer (blue dot curve), and tetralayer (green short-dash curve) phosphorene. (Right) Initial wave-packet energy for the corresponding initial wave vector assumed here in the wave-packet simulation. θ_k as a function of (c) the polar angle β for fixed momentum vector and (d) the momentum vector for fixed polar angle β. (e) Momentum value for $\theta_{\max}$ as a function of the polar angle β, i.e., $|k|$ in which θ_k has a maximum value as emphasized in the orange dashed line in panel (d).

where $u_0^n = u_0 + \lambda_n \delta_{AD'}$, $\eta_x^n = \eta_x + \lambda_n \eta_{AD'}$, $\eta_y^n = \eta_y + \lambda_n \gamma_{AD'}$, $\delta^n = \delta + \lambda_n \delta_{AC'}$, $\gamma_x^n = \gamma_x + \lambda_n \eta_{AC'}$, $\gamma_y^n = \gamma_y + \lambda_n \gamma_{AC'}$, $\chi^n = \chi + \lambda_n \chi_{AC'}$, $\lambda_n = \cos[n\pi/(N+1)]$, N is the number of BP layers and $n \in [1, N]$. The lowest electron-hole energy bands are obtained by assuming $n = N$, being the value we consider here throughout all our analysis (i.e., $n = N = 1$, 2, 3, 4 for monolayer, bilayer, trilayer, and tetralayer phosphorene, respectively). The Hamiltonian parameter values are summarized in Table I, being the same ones used in Ref. [69], where they were obtained by expanding the tight-binding structure factors for BP system up to second oder in k. These coefficient values of the Hamiltonian (1) include the contribution from the tight-binding hopping energies and the lattice geometry of the BP sheet, incorporating a direct link between the microscopic tight-binding description and the continuum approximation. References [69,79,80] have showed that the continuum model for BP system is very suited for describing the physics of large BP systems, yielding very accurate results within its limit of validation, and it is less computationally demanding than microscopic models, as for instance tight-binding model and first-principles calculations.

The eigenstates of $\mathcal{H}$ are two-component spinors given by

$$\Psi = \begin{pmatrix} \phi_1 \\ \phi_2 \end{pmatrix} = \begin{pmatrix} \phi_A + \phi_D \\ \phi_B + \phi_C \end{pmatrix}, \tag{2}$$

TABLE I. Hamiltonian parameters of the effective continuum model [Eq. (1)] derived by the expansion of the structure factor coefficients of the tight-binding model for multilayer BP (see Ref. [69]).

Parameter	Value	Parameter	Value
u_0	−0.414 eV	$\delta_{AC'}$	0.712 eV
η_x	1.265 eV Å^2	$\delta_{AD'}$	−0.132 eV
η_y	−1.384 eV Å^2	$\eta_{AC'}$	−0.9765 eV Å^2
δ	0.919 eV	$\eta_{AD'}$	2.699 eV Å^2
γ_x	2.510 eV Å^2	$\gamma_{AC'}$	2.443 eV Å^2
γ_y	2.035 eV Å^2	$\gamma_{AD'}$	0.364 eV Å^2
χ	5.896 eV Å	$\chi_{AC'}$	2.071 eV Å

where $\phi_{A,B,C,D}$ are the probability amplitudes for finding electrons on the atomic sites A, B, C, and D, respectively, which are related to the four phosphorus atoms that are contained in the unit cell of a single layer of BP, as shown in Fig. 1(a). The Hamiltonian (1) was obtained by taking into account the sublattice symmetry between atomic sites A/D and B/C in each monolayer BP, due to the D_{2h} group invariance of the BP lattice [69,79] and, as a consequence, the two-component wave function (2) is composed by the combination of these sublattices in pairs. Rewriting $\mathcal{H}$ in a more compact form in polar notation, in order to highlight the angular dependence, we find

$$\mathcal{H} = \begin{pmatrix} \varepsilon_1 & \varepsilon_2 e^{i\theta_k} \\ \varepsilon_2 e^{-i\theta_k} & \varepsilon_1 \end{pmatrix}, \tag{3}$$

with

$$\varepsilon_1(\vec{p}) = \frac{f_c + f_v}{2}, \tag{4a}$$

$$\varepsilon_2(\vec{p}) = \sqrt{\left(\frac{f_c - f_v}{2}\right)^2 + \left(\frac{\chi^n p_y}{\hbar}\right)^2}, \tag{4b}$$

$$\theta_k(\vec{p}) = \arctan\left[\frac{2\chi^n p_y}{\hbar(f_c - f_v)}\right], \tag{4c}$$

where f_c and f_v are associated with the conduction (c) and valence (v) energy dispersion terms, respectively, being defined as

$$f_{\substack{c \\ v}} = \left(u_0^n \pm \delta^n\right) + \left(\eta_x^n \pm \gamma_x^n\right)\frac{p_x^2}{\hbar^2} + \left(\eta_y^n \pm \gamma_y^n\right)\frac{p_y^2}{\hbar^2}. \tag{5}$$

By diagonalizing Eq. (1) or equivalently Eq. (3), we obtain the dispersion relations for electrons and holes, given by

$$E_{\vec{p},s} = \varepsilon_1(\vec{p}) + s\varepsilon_2(\vec{p}), \tag{6}$$

with $s = +1(-1)$ for electrons (holes), i.e., the plus (minus) sign yields the conduction (valence) band. Figure 1(b) shows the lowest electronic energy levels for (black solid curve, $N = 1$) monolayer, (red dashed curve, $N = 2$) bilayer, (blue dot curve, $N = 3$) trilayer, and (green short-dash curve, $N = 4$) tetralayer phosphorene. In the wave-packet dynamics, we choose the initial wave-packet energies for electrons standing on these lower bands, as shown in the right panel of Fig. 1(b) for the three assumed initial wave vectors for a fixed number of layers. Note that, as seen in Fig. 1(b): (i) the band gap is tunable by the number of BP layers, decreasing as N increases, and (ii) phosphorene band structure is highly anisotropic, exhibiting for small momentum values an approximately parabolic dispersion along Γ-X (zigzag) direction and approximately linear dispersion along Γ-Y (armchair) direction, therefore, behaving similarly as Schrödinger and Dirac particles, respectively. As we will discuss further, the linear dependence on k_y in the out-of-diagonal terms of Eq. (1) and this anisotropic feature of the energy levels and, consequently, of effective masses and group velocities [69], bring up very interesting consequences in the wave-packet dynamics in phosphorene.

The corresponding eigenstates of Hamiltonian (3) are

$$\Psi_{\vec{p},s} = \frac{1}{\sqrt{2}}\begin{pmatrix} 1 \\ s e^{i\theta_k(\vec{p})} \end{pmatrix}. \tag{7}$$

Note that this expression is similar to the graphene's eigenstates [43], but with the fundamental difference that for N-layer phosphorene the phase angle θ_k does not necessarily correspond to the polar angle β associated with the momentum vector:

$$\theta_k(|k|, \beta) = \arctan\left[\frac{\chi^n |k| \sin\beta}{\delta^n + \left(\gamma_x^n \cos^2\beta + \gamma_y^n \sin^2\beta\right)|k|}\right]. \tag{8}$$

This can be seen in Fig. 1(c), which shows the phase angle θ_k as a function of the polar angle β for three different momentum vectors (whose values are the ones used in the results for the wave-packet simulation in Sec. III). It is a very crucial point concerning the initial set up to define the direction of the wave-packet propagation. For instance, in the cases of isotropic semiconductors and graphene systems [43,54,81,82], the phase angle is exactly the same as the polar angle in the momemtum space, i.e., $\theta_k = \beta = \arctan(p_y/p_x)$, making the definition of the initial propagation angle value more direct and intuitive. Furthermore, it can be noticed by Fig. 1(c) that θ_k exhibits a maximum value at $\beta = \pi/2$ for all momentum values and this critical value $\theta_k(\beta = \pi/2) = \theta_k^{\max}$ is energy-momentum-dependent. Figures 1(d) and 1(e) confirm these statements. From Fig. 1(d), it is seen that, as the momentum $|k|$ increases, θ_k approaches a maximum value (emphasized by the orange dashed line) and then decays to zero. The momentum value for $\theta_k^{\max}$ (i.e., $|k|_{\max}$ in which θ_k has a maximum value) is slightly different for different values of the polar angle β, as shown in Fig. 1(e). According to Fig. 1(e) and also by performing the differentiation of Eq. (4c) with respect to $|k|$ at $\beta = \pi/2$, i.e., $(\partial\theta_k/\partial|k|)|_{\beta=\pi/2} = 0$, one can find that $|k|_{\max} = 0.67201\,\text{Å}^{-1}$ and the critical phase angle is $\theta_k^{\max} = 65.114^\circ$. In summary, the phase angle can assume values in the threshold range between: $-\theta_k^{\max} \leqslant \theta_k \leqslant \theta_k^{\max}$, unlike the polar angle β that can assume any value.

B. Green's function formalism for N-layer phosphorene

We now shall follow a similar procedure as reported by Maksimova *et al.* in Ref. [43], based on the Green's function formalism. According to Eq. (7), the time-dependent eigenfunctions of Hamiltonian Eq. (3) are given by

$$\varphi_{\vec{p},s}(\vec{r}, t) = \frac{1}{2\sqrt{2\pi}} \exp\left[i\frac{\vec{p}\cdot\vec{r}}{\hbar} - i\frac{E_{\vec{p},s}t}{\hbar}\right]\begin{pmatrix} 1 \\ s e^{i\theta_k(\vec{p})} \end{pmatrix}, \tag{9}$$

with $E_{\vec{p},s}$ being the energy eigenvalues given in Eq. (6). The initial wave packet $\Psi(\vec{r}, 0)$ at $t > 0$ acquires a form that can be calculated as

$$\Psi_\mu(\vec{r}, t) = \int G_{\mu,\nu}(\vec{r}, \vec{r}', t)\Psi_\nu(\vec{r}', 0)\, d\vec{r}', \tag{10}$$

where $G(\vec{r}, \vec{r}', t)$ is the 2×2 Green's function matrix and the matrix indices ($\mu, \nu = 1, 2$) correspond to the two components of the pseudospin eigenfunctions. The matrix elements

of Green's functions are defined as

$$G_{\mu,\nu}(\vec{r},\vec{r'},t)=\sum_{s=\pm1}\int d\vec{p}\varphi_{\vec{p},s,\mu}(\vec{r},t)\varphi^{*}_{\vec{p},s,\nu}(\vec{r'},0). \tag{11}$$

Replacing Eq. (9) into Eq. (11) and after some straightforward algebra, one finds the components of Green's function matrix, such as

$$G_{11}(\vec{r},\vec{r'},t)=G_{22}(\vec{r},\vec{r'},t)=\frac{1}{(2\pi\hbar)^2}\int\exp\left[\frac{i\vec{p}\cdot(\vec{r}-\vec{r'})}{\hbar}\right]\exp\left[\frac{-i\varepsilon_1(\vec{p})t}{\hbar}\right]\cos\left[\frac{\varepsilon_2(\vec{p})t}{\hbar}\right]d\vec{p}, \tag{12a}$$

$$G_{12}(\vec{r},\vec{r'},t)=\frac{-i}{(2\pi\hbar)^2}\int e^{-i\theta_k(\vec{p})}\exp\left[\frac{i\vec{p}\cdot(\vec{r}-\vec{r'})}{\hbar}\right]\exp\left[\frac{-i\varepsilon_1(\vec{p})t}{\hbar}\right]\sin\left[\frac{\varepsilon_2(\vec{p})t}{\hbar}\right]d\vec{p}, \tag{12b}$$

$$G_{21}(\vec{r},\vec{r'},t)=\frac{-i}{(2\pi\hbar)^2}\int e^{i\theta_k(\vec{p})}\exp\left[\frac{i\vec{p}\cdot(\vec{r}-\vec{r'})}{\hbar}\right]\exp\left[\frac{-i\varepsilon_1(\vec{p})t}{\hbar}\right]\sin\left[\frac{\varepsilon_2(\vec{p})t}{\hbar}\right]d\vec{p}. \tag{12c}$$

To describe the time evolution of an arbitrary state, we choose the initial wave function to be a Gaussian wave packet, for three main reasons: (i) Gaussian wave packets describe roughly localized quantum states for which the product of the uncertainties in position and momentum is minimal; (ii) by setting the initial state as Gaussian wave packet, this situation covers most cases of practical interest, because any wave packet can be approximated by a superposition of a finite number of Gaussian states; and (iii) since the ZBW is, by nature, not a stationary state but a dynamical phenomenon, it is natural to study it with the use of wave packets [1,23,46]. The assumed initial Gaussian wave packet, with width d and nonvanishing average momentum along y-direction ($p_{0y}=\hbar k_0$), is given by

$$\Psi(\vec{r},t)=\frac{f(\vec{r})}{\sqrt{|c_1|^2+|c_2|^2}}\begin{pmatrix}c_1\\c_2\end{pmatrix}, \tag{13a}$$

$$f(\vec{r})=\frac{1}{d\sqrt{\pi}}\exp\left[\frac{-r^2}{2d^2}+ik_0y\right]. \tag{13b}$$

where c_1 and c_2 determine the initial pseudospin polarization of the injected wave packet and are related to the two pseudospin components in Eqs. (2) and (7). Now inserting Eqs. (13a) and (13b) into Eq. (10) and using the expressions of the components of Green's function matrix [Eqs. (12a)–(12c)], one obtains the components of the time evolved wave packet $\Psi(\vec{r},t)$ at a later time t in the following two-component form:

$$\begin{pmatrix}\Psi_1(\vec{r},t)\\\Psi_2(\vec{r},t)\end{pmatrix}=\frac{1}{\sqrt{|c_1|^2+|c_2|^2}}\begin{pmatrix}c_1\Phi_1(\vec{r},t)+c_2\Phi_3(\vec{r},t)\\c_1\Phi_2(\vec{r},t)+c_2\Phi_4(\vec{r},t)\end{pmatrix}, \tag{14}$$

where

$$\Phi_1(\vec{r},t)=\int G_{11}(\vec{r},\vec{r'},t)f(\vec{r})d\vec{r'}=\frac{de^{-k_0^2d^2/2}}{2\hbar^2\sqrt{\pi^3}}\int\exp\left[\frac{i\vec{p}\cdot\vec{r}}{\hbar}-\frac{p^2d^2}{2\hbar^2}+\frac{p_yk_0d^2}{\hbar}-\frac{i\varepsilon_1(\vec{p})t}{\hbar}\right]\cos\left(\frac{\varepsilon_2(\vec{p})t}{\hbar}\right)d\vec{p}, \tag{15a}$$

$$\Phi_2(\vec{r},t)=\int G_{21}(\vec{r},\vec{r'},t)f(\vec{r})d\vec{r'}=\frac{-ide^{-k_0^2d^2/2}}{2\hbar^2\sqrt{\pi^3}}\int e^{i\theta_k(\vec{p})}\exp\left[\frac{i\vec{p}\cdot\vec{r}}{\hbar}-\frac{p^2d^2}{2\hbar^2}+\frac{p_yk_0d^2}{\hbar}-\frac{i\varepsilon_1(\vec{p})t}{\hbar}\right]\cos\left(\frac{\varepsilon_2(\vec{p})t}{\hbar}\right)d\vec{p}, \tag{15b}$$

$$\Phi_3(\vec{r},t)=\int G_{12}(\vec{r},\vec{r'},t)f(\vec{r})d\vec{r'}=\frac{-ide^{-k_0^2d^2/2}}{2\hbar^2\sqrt{\pi^3}}\int e^{-i\theta_k(\vec{p})}\exp\left[\frac{i\vec{p}\cdot\vec{r}}{\hbar}-\frac{p^2d^2}{2\hbar^2}+\frac{p_yk_0d^2}{\hbar}-\frac{i\varepsilon_1(\vec{p})t}{\hbar}\right]\cos\left(\frac{\varepsilon_2(\vec{p})t}{\hbar}\right)d\vec{p}, \tag{15c}$$

and $\Phi_1(\vec{r},t)=\Phi_4(\vec{r},t)$, according to Eq. (12a).

The time-dependent expectation value of the position operator can be calculated as

$$\langle\vec{r}(t)\rangle=\sum_{j=1}^{2}\int d\vec{p}\Psi_j^{*}(\vec{p},t)i\hbar\frac{d\Psi_j(\vec{p},t)}{d\vec{p}}, \tag{16}$$

with Ψ in momentum representation. Note that analytical expressions for two components of wave function were found for N-layer BP [Eqs. (14) and (15a)–(15c)], which allows us to investigate the ZBW phenomenon of a Gaussian wave packet for different relations between the initial electron amplitudes on the sublattices, as will be discussed in Sec. III, by means of the analytical calculation of the time dependent expectation values of the position (x, y) of the center of the injected wave packet according to Eq. (16).

C. Split-operator technique for *N*-layer phosphorene

In this section, we introduce the split-operator technique for wave-packet propagation in N-layer phosphorene, based on the Hamiltonian within the continuum approximation [Eq. (1)]. This approach is similar to the one developed by A. Chaves *et al.* [54,81,83] for calculating the dynamics of a

wave packet in graphene by taking a Dirac-Weyl Hamiltonian. It consists in the solution of time-dependent Schrödinger equation by taking a separation of the time-evolution operator in a series of matrices, such that the propagated wave function after a time step Δt can be calculated by applying the expanded exponential time-evolution operator on the wave packet at any instant t [54,81–93]. The advantage of this technique is due to its flexibility inasmuch as it can be applied for BP systems under arbitrary external potentials and magnetic fields. Besides, it allows to track the center of mass trajectories, which is very important for the understanding of ZBW phenomenon in the current work.

Let us first find the time-evolution operator as a series of matrix multiplications for the Hamiltonian (1) and then apply it for the time evolution of the wave packet, following the split-operator method for spin-dependent Hamiltonian as described in Refs. [54,81,83]. The long-wavelength Hamiltonian (1) can be written in terms of Pauli matrices $\vec{\sigma} = (\sigma_x, \sigma_y)$ as

$$\mathcal{H} = \mathcal{H}_0 \mathbb{1} + \vec{\alpha} \cdot \vec{\sigma}, \tag{17}$$

where $\mathbb{1}$ denotes the 2×2 unit matrix, and

$$\mathcal{H}_0 = u_0^n + \eta_x^n k_x^2 + \eta_y^n k_y^2, \tag{18a}$$

$$\vec{\alpha} = (\alpha_x, \alpha_y) = \left(\delta^n + \gamma_x^n k_x^2 + \gamma_y^n k_y^2, -\chi^n k_y\right). \tag{18b}$$

Since $\mathcal{H}$ does not explicitly depend on time and $[\mathcal{H}_0 \mathbb{1}, \vec{\alpha} \cdot \vec{\sigma}] = 0$, the time-evolution operator for the Hamiltonian Eq. (17) is given by

$$\exp\left[-\frac{i}{\hbar}\mathcal{H}\Delta t\right] = \exp\left[-\frac{i}{\hbar}\mathcal{H}_0 \mathbb{1}\Delta t\right] \exp[-i\vec{A} \cdot \vec{\sigma}], \tag{19}$$

where $\vec{A} = \vec{\alpha}\Delta t/\hbar$. Using the properties of the Pauli matrices for the second term in Eq. (19), one finds

$$\begin{aligned} \mathcal{M}_A &= \exp[-i\vec{A} \cdot \vec{\sigma}] \\ &= \cos(A)\mathbb{1} - \frac{i\sin(A)}{A}\begin{pmatrix} 0 & A_x - iA_y \\ A_x + iA_y & 0 \end{pmatrix}, \end{aligned} \tag{20}$$

where $A = |\vec{A}|$, whereas the first term of Eq. (19) is equivalent to

$$\mathcal{M}_{\mathcal{H}_0} = \exp\left[-i\mathcal{H}_0 \mathbb{1}\Delta t/\hbar\right] = \mathbb{1}\exp\left[-i\mathcal{H}_0 \Delta t\hbar\right]. \tag{21}$$

Thus the time-evolution operation is represented by a simple multiplication of two 2×2 matrices. Notice that this resulting matrix is an exact representation of the time-evolution operator, including all the terms of the expansion of the exponential, and that there is no error induced by the noncommutativity of the involved operators. Although no approximation was taken, we refer this method as the split-operator technique due to the similarities in the development of the method as in Refs. [54,81,83], and also because we in fact are splitting the time-evolution operator.

The time evolution of $\Psi(\vec{r}, t)$ can be computed by applying the time-evolution operator Eq. (19) to obtain the propagated wave function after a time step $t + \Delta t$, such as

$$\Psi(\vec{r}, t + \Delta t) = e^{-i\mathcal{H}\Delta t/\hbar}\Psi(\vec{r}, t) = \mathcal{M}_A \mathcal{M}_{H_0}\Psi(\vec{r}, t). \tag{22}$$

Since $\mathcal{M}_{\mathcal{H}_0}$ and $\mathcal{M}_A$ depend on the wave vectors k_x and k_y, the matrix multiplication is computed in reciprocal space by performing a Fourier transform on the wave function, in order to rewrite it in a space where the k's are numbers, instead of derivatives.

The initial wave packet is assumed as a circularly symmetric Gaussian distribution, multiplied by the pseudospinor [Eq. (2)] that accounts for the probability distributions over the two pairs of coupled sublattices of phosphorene (labeled c_1 for $\phi_A + \phi_D$ and c_2 for $\phi_B + \phi_C$), and by a plane wave with wave vector $\vec{k} = (k_0 \cos\beta, k_0 \sin\beta)$, such as

$$\Psi(\vec{r}, 0) = N\begin{pmatrix} c_1 \\ c_2 \end{pmatrix} \exp\left[-\frac{(x - x_0)^2 + (y - y_0)^2}{d^2} + i(\vec{k} \cdot \vec{r})\right], \tag{23}$$

where N is a normalization factor, (x_0, y_0) are the coordinates of the center of the Gaussian wave packet in the real space, and d is its width. The pseudospin polarization $[c_1, c_2]^T$ of the wave packet plays an important role in defining the direction of propagation [see Eq. (7)]. It is worth to point out that, for phosphorene, the phase angle θ_k does not correspond to the polar angle β associated with the momentum vector [see Eq. (8)], such that the characterization of the pseudospin polarization angle and consequently the direction of propagation are not directly related, as it is, for example, in graphene, where we have a wave packet propagating along the y and x direction in cases of the pseudospin $[1, i]^T$ and $[1, 1]^T$, respectively [81,82,89,90,93]. Unless otherwise explicitly stated in the text, we consider that the wave packet starts at $(x_0, y_0) = (0, 0)$ Å and its width is $d = 100$ Å. In order to compare the results obtained by the method based on split-operator technique developed in the current section with the ones within the Green's function formalism (Sec. II B), we assume $k_0^x = 0$ in Eq. (23) as in Eq. (13b). The assumed time step for all obtained results here in both approaches is $\Delta t = 0.1$ fs.

III. ZITTERBEWEGUNG OF GAUSSIAN WAVE PACKET FOR DIFFERENT PSEUDOSPIN POLARIZATIONS

Let us now show results for three different Gaussian distributions along the subalttices: (Sec. III A) $[c_1, c_2]^T = [1, 0]^T$, (Sec. III B) $[c_1, c_2]^T = [1, 1]^T$, and (Sec. III C) $[c_1, c_2]^T = [1, i]^T$, where we discuss the presence or absence of ZBW along the x and y directions, manifested by oscillations on the average position and average group velocity of the Gaussian center of mass of the wave packet, as well as other features of the trembling motion, such as the oscillation amplitude and frequency.

A. $c_1 = 1$ and $c_2 = 0$

We first consider the simple case where the lower component of the initial electronic wave function (13a) is zero, i.e., taking $c_1 = 1$ and $c_2 = 0$. This corresponds to the situation in which the electron probability is initially located only at $\phi_1 = \phi_A + \phi_C$, i.e., at the A and C the sublattices of phosphorene layer. According to Eq. (14), the wave function for $t > 0$ in this case is

$$\Psi(\vec{r}, t) = \begin{pmatrix} \Phi_1(\vec{r}, t) \\ \Phi_2(\vec{r}, t) \end{pmatrix}, \tag{24}$$

where $\Phi_{1,2}$ are defined by Eqs. (15a) and (15b). By using Eq. (16) and after some lengthy but straightforward algebra, we calculate the time dependent expectation value of position (x, y) of the wave-packet center of mass, given by

$$\langle x(t)\rangle = -\frac{ide^{-a^2}}{\pi}\int_0^{\infty}\int_{-\pi}^{\pi} e^{-q^2+2aq\sin\beta}\left[\frac{2i\chi^n\gamma_x^n\hbar^4 dq^3\sin(2\beta)\sin^2(\varepsilon_2(q,\beta)t/\hbar)}{\left[\delta^n\hbar^2d^2+\left(\gamma_x^n\cos^2\beta+\gamma_y^n\sin^2\beta\right)q^2\hbar^2\right]^2+d^2(\chi^n)^2\hbar^4q^2\sin^2\beta}\right.$$
$$\left.+\frac{2it\eta_x^nq^2\cos\beta}{\hbar d^2}+q^2\cos\beta\right]d\beta dq, \tag{25a}$$

$$\langle y(t)\rangle = -\frac{ide^{-a^2}}{\pi}\int_0^{\infty}\int_{-\pi}^{\pi} e^{-q^2+2aq\sin\beta}\left[-\frac{iq\chi^n\hbar^2d\left(d^2\delta^n\hbar^2+\gamma_x^nq^2\hbar^2\cos^2\beta-\gamma_y^nq^2\hbar^2\sin^2\beta\right)\sin^2(\varepsilon_2(q,\beta)t/\hbar)}{\left[\delta^n\hbar^2d^2+\left(\gamma_x^n\cos^2\beta+\gamma_y^n\sin^2\beta\right)q^2\hbar^2\right]^2+d^2(\chi^n)^2\hbar^4q^2\sin^2\beta}+q^2\sin\beta\right.$$
$$\left.-aq+\frac{2it\eta_y^nq^2\sin\beta}{\hbar d^2}\right]d\beta dq, \tag{25b}$$

in which the average values are written explicitly as a function of the polar angle $\beta\in[-\pi,\pi]$ and the dimensionless parameters $q = pd/\hbar$ and $a = k_0d$, with k_0 corresponding to the initial wave vector. For this, we rewrote ε_1 and ε_2, given by Eqs. (4a) and (4b), respectively, as functions of q and β.

By performing a numerical integration of Eqs. (25a) and (25b), we obtain the expectation values as a function of time for different initial central wave vectors and number of BP layers, as shown in Figs. 2(a) and 2(b), respectively. The average value $\langle x(t)\rangle$ remains constant and does not exhibit any oscillation with time for different k's values and number of BP layers. On the other hand, the expectation value of the y position of the wave packet oscillates, thus indicating the presence of ZBW along the y direction. The different curves in Fig. 2(a) are the results for $k_0 = 0.01$ (black), 0.05 (red) and 0.1 Å^{-1} (blue). As mentioned in Sec. I, this oscillatory behavior is due to the interference between positive and negative energy-momentum states that makes up the initial Gaussian wave packet and in fact corresponds to the ZBW phenomenon. Note in Fig. 2(a) that the ZBW of the wave packet propagating in a monolayer BP have a transient character, i.e., they disappear on a femtosecond timescale. This transient feature of the ZBW presents different amplitude, frequency and duration time for different initial wave vector. One verifies in Fig. 2(a) that (i) the duration time and amplitude of the transient ZBW decays faster as the wave vector increases and (ii) the larger the initial wave vector, the smaller the oscillation amplitude, as seen in the inset of panel (a). Both features are consequences of the effect of wave-packet dispersion. It is worth to mention that the transient oscillation time due to the ZBW effect is shorter than the lifetimes of excited electrons in standard semiconductors. According to the Refs. [43,46,49,54], ZBW has a transient character with a decay time of femtoseconds in graphene and picoseconds in nanotubes, whereas excited electrons have lifetime, given by the Fermi's gold rule, of a few nanoseconds [95]. Similarly, we found that the ZBW transient behavior for phosphorene is also in the order of dozens of femtoseconds.

We also analyze the influence of the number of layers on the wave-packet propagation. Results are shown in Fig. 2(b) for $N = 1, 2, 3, 4$, considering a fixed value $k_0 = 0.1$ Å^{-1}. One observes that increasing the number of layers causes a reduction (increase) of the frequency (period) of the transient oscillation. This is related to the fact that multilayer BP with different numbers of BP layers presents slightly different

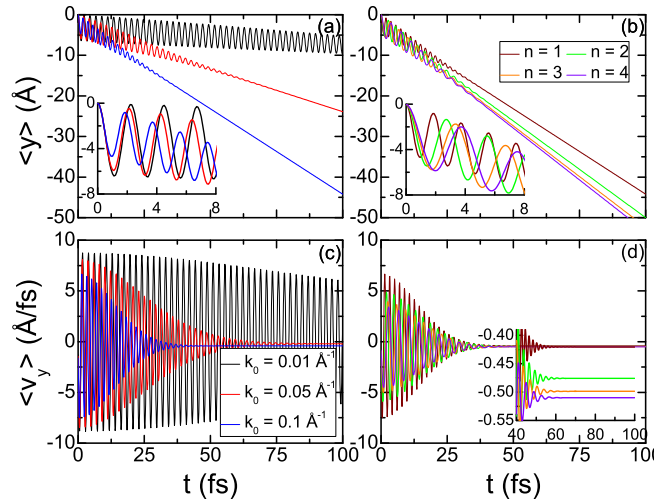

FIG. 2. [(a) and (b)] Average position and [(c) and (d)] expectation value of the velocity for trajectories of (a) and (b), respectively, of a Gaussian wave packet of width $d = 100$ Å as a function of time for the case $c_1 = 1$ and $c_2 = 0$. [(a) and (c)] Wave packet propagating in a monolayer phosphorene sheet ($N = 1$) with different initial central wave vectors: $k_0 = 0.01$ (black), 0.05 (red) and 0.1 Å^{-1} (blue). [(b) and (d)] Wave packet propagating in multilayer phosphorene ($N = 1, 2, 3, 4$) for fixed wave vector $k_0 = 0.1$ Å^{-1}. The wave packet starts at $(x_0, y_0) = (0, 0)$ Å. The inset shows an enlargement of the physical averages [(a) and (b)] for first time steps in order to emphasize the different oscillation amplitudes and oscillation frequencies, and (d) nearby the time steps in which the velocities achieve constant values.

energy band structures and consequently different effective masses along x and y directions, as discussed in Sec. II A. It is known that the greater the number of layers, the greater (smaller) will be the effective mass for electrons along the x (y) direction, i.e., along the zigzag (armchair) directions.[69] That in turn affects the mobility of electrons located on the lowest conduction band, leading to a phase difference in the oscillation of the average position $\langle y(t)\rangle$ for different number of layers N. By comparing Figs. 2(a) and 2(b), one verifies that the oscillatory behavior for multilayer BP is qualitatively similar to monolayer case, except by this phase difference in the ZBW, as emphasized in the inset of Fig. 2(b), due to the different energy band curvatures as the number of layers BP.

Since the oscillatory behavior of the propagation velocity as a function of time is also a manifestation of the ZBW effect, we show in Figs. 2(c) and 2(d) the expectation values of the velocity v_y for average position y of panels (a) and (b), respectively, calculated by taking the time derivative of the $\langle y(t)\rangle$ results with respect to time. Note that the average velocities exhibit clear oscillations that are damped as time evolves, converging to a final constant value that depends on the initial wave vector k_0 and number of considered BP layers. The velocity wiggles with shorter period and smaller amplitudes for large values of k_0 and fixed number N [see Fig. 2(c)], as well as for large number of layer and fixed k_0 [see inset in Fig. 2(d)]. The convergence of the velocities demonstrates that the ZBW is not a permanent but a transient effect. Notice from the inset in Fig. 2(d) that the converging value of $\langle v_y\rangle$ has slightly larger module for larger N. This is related to the fact that the lowest energy band along Γ-Y direction for multilayer BP has approximately the same curvatures for different number of layers, and consequently the effective masses for electrons along y-direction are just slightly different for different layers, as can be seen by the following values: $m_1^y = 0.19474m_0$, $m_2^y = 0.18835m_0$, $m_3^y = 0.17088m_0$, and $m_4^y = 0.15648m_0$, being m_0 the mass of a free electron, and thus leading also to a slight difference in the electronic mobility and group velocity in y direction [69].

Figure 3 shows the contour plots of the squared modulus of the propagated wave functions at (a) $t = 20$, (b) 30, (c) 40, and (d) 50 fs, considering an initial wave vector $k_0 = 0.05$ Å^{-1} that corresponds the average position of the electron wave-packet motion displayed by the red curve in Fig. 2(a). It is seen that the time evolution of the electronic wave packet for this case is along the armchair (y) direction. Starting with a circularly symmetric shape, the wave packet evolves and becomes distorted into an elliptic shape. This is due to the strong anisotropy in multilayer phosphorene, such that the momentum contributions along the (y) armchair and (x) zigzag directions to the total momentum are different, thus giving rise to elliptic probability distribution, as shown in Fig. 3(a). For a large enough time, the wave packet splits in two parts at $t \approx 50$ fs [Fig. 3(d)] moving along y axis with opposite velocities so that the electron probability density is almost symmetrical with respect to y at a fixed time step: $|\Psi(x, y, t)|^2 \approx |\Psi(x, -y, t)|^2$. It should be noticed that the two subpackets are definitely not completely symmetric, otherwise we would not have a non-null average position in the y direction and a total propagation evolving to negative values of y, as shown in Figs. 2(a) and 2(b). The two propagating subpackets

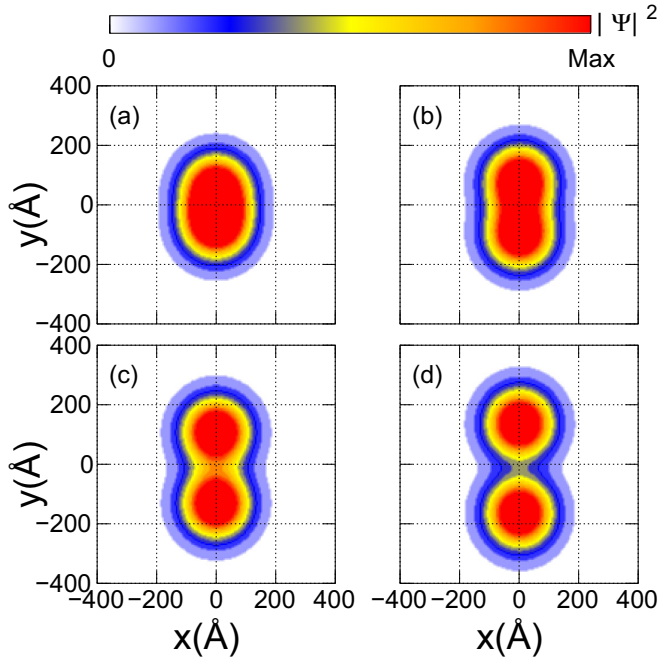

FIG. 3. Time evolution of the electronic wave packet for the case $[c_1, c_2]^T = [1, 0]^T$ with $|k| = 0.05$ Å^{-1}, corresponding the average position shown by the red curve in Fig. 2(a). Snapshots at (a) $t = 20$, (b) 30, (c) 40 and (d) 50 fs.

with approximately the same probability densities and widths lead to vanishing oscillations in the average position and expectation values of velocity, as verified by the red curves in Figs. 2(a) and 2(c) after $t \approx 85$ fs, which explains the transient behavior of the ZBW and the fact that the average velocity converges to values close to zero. Although not shown here, it is intuitive that for higher wave vectors, the wave packet splitting (into two) should take place earlier. As a consequence, the average velocity would display a faster decay rate and a shorter oscillation time transient.

In contrast to the results shown in Fig. 2 for the given initial polarization $[1, 0]^T$ of wave packet propagating in multilayer BP, the ZBW for monolayer graphene [43,54] and bilayer graphene [46] occurs in the direction perpendicular to the initial momentum k_0^y, i.e., for initial polarization $[1, 0]^T$ the wave packet propagates along x direction in which exhibits ZBW effect, whereas $\langle y(t)\rangle$ remains constant. This is counter-intuitive, since the initial momentum along x direction is null as in Eq. (13b). However, similar to Fig. 3, in graphene the wave function also is found to split in two subpackets along the y direction [43]. This different direction of propagation between the multilayer BP and those reported for monolayer and bilayer graphene in Refs. [43,46,54] can be understood considering the fact that, since the direction of propagation y is the crystallographic direction in the phosphorene in which electrons have greater (lower) kinetic energy (effective mass), then electrons have greater mobility along the y direction, being its preferred direction of propagation.

B. $c_1 = 1$ and $c_2 = 1$

We now investigate the case in which the wave function is equally distributed in the combined sublattices A/C

(correspoding to ϕ_1) and B/D (correspoding to ϕ_2), which is equivalent as choosing $c_1 = 1$ and $c_2 = 1$ in Eq. (14), resulting in

$$\Psi(\vec{r},t) = \frac{1}{\sqrt{2}}\begin{pmatrix}\Phi_1(\vec{r},t) + \Phi_3(\vec{r},t)\\ \Phi_1(\vec{r},t) + \Phi_2(\vec{r},t)\end{pmatrix}, \tag{26}$$

where $\Phi_{1,2,3}$ are defined by Eqs. (15a)–(15c). Note that an initial wave packet in which the electron probability density occupies equally all subllatices is more realistic experimentally, as an expected configuration when one creates wave packets by illuminating samples with short laser pulses [96] and also because for an infinite system the initial wave function should describe electronic bulk states spread over all sites around the center point of the Gaussian distribution. On the other hand, the simplistic choice $[1,0]^T$ of the initial wave packet discussed in previous Sec. III A is widely used in the literature [43,46,54], since it is amenable to analytical treatment and gives valuable insight into the relevant timescales of the problem. In addition, for the phosphorene case, the initial configuration $[1,0]^T$ can be seen as the representation of quasiflat edge states in phosphorene nanoribbons with zigzag edges that have nonzero wave function components just in one of the coupled pairs A/D or B/C [80]. Replacing the wave function Eq. (26) into Eq. (16), we find the following expressions for the average positions in x and y directions:

$$\langle x(t)\rangle = -\frac{ie^{-a^2}}{\pi}\int_0^\infty\int_{-\pi}^{\pi} e^{-q^2+2aq\sin\beta}\left\{\frac{i\chi^n\gamma_x^n\hbar^4d^2q^3\sin(2\beta)\sin\left(2\varepsilon_2(q,\beta)t/\hbar\right)\sin\theta_k(q,\beta)}{\left[\delta^n\hbar^2d^2+\left(\gamma_x^n\cos^2\beta+\gamma_y^n\sin^2\beta\right)q^2\hbar^2\right]^2+d^2(\chi^n)^2\hbar^4q^2\sin^2\beta}\right.$$
$$+dq^2\cos\beta+\frac{2it\eta_x^nq^2\cos\beta}{\hbar d}+\left[\sin\left(\frac{2\varepsilon_2(q,\beta)t}{\hbar}\right)-i\cos\theta_k(q,\beta)\cos\left(\frac{2\varepsilon_2(q,\beta)t}{\hbar}\right)\right]$$
$$\left.\times\left[\frac{2t\left[\delta^n\hbar^2d^2+\left(\gamma_x^n\cos^2\beta+\gamma_y^n\sin^2\beta\right)q^2\hbar^2\right]\gamma_x^nq^2\cos\beta}{\hbar^3d^3\varepsilon_2(q,\beta)}\right]\right\}d\beta dq, \tag{27a}$$

$$\langle y(t)\rangle = -\frac{ie^{-a^2}}{\pi}\int_0^\infty\int_{-\pi}^{\pi} e^{-q^2+2aq\sin\beta}\left\{-\frac{iq\chi^n\hbar^2d^2\left[\delta^n\hbar^2d^2+\left(\gamma_x^n\cos^2\beta-\gamma_y^n\sin^2\beta\right)q^2\hbar^2\right]\sin\left(2\varepsilon_2(q,\beta)t/\hbar\right)\sin\theta_k(q,\beta)}{\left[\delta^n\hbar^2d^2+\left(\gamma_x^n\cos^2\beta+\gamma_y^n\sin^2\beta\right)q^2\hbar^2\right]^2+d^2(\chi^n)^2\hbar^4q^2\sin^2\beta}\right.$$
$$-adq+dq^2\sin\beta+\frac{2it\eta_y^nq^2\sin\beta}{\hbar d}+itq^2\cos\theta_k(q,\beta)$$
$$\left.\times\left[\frac{2\gamma_x^n\cos\beta\left[\delta^n\hbar^2d^2+\left(\gamma_x^n\cos^2\beta+\gamma_y^n\sin^2\beta\right)q^2\hbar^2\right]+(\chi^n)^2\hbar^2d^2\sin\beta}{\hbar^3d^3\varepsilon_2(q,\beta)}\right]\right\}d\beta dq, \tag{27b}$$

with θ_k, $\varepsilon_{1,2}$ written explicitly as a function of the polar angle β and the dimensionless parameters q [see Eq. (8)].

Similarly to the previous Sec. III A for the pseudospin $[1,0]^T$, in the current case the average value $\langle x(t)\rangle$ is also unchanged with time, whereas the expectation value of the y position oscillates. These results are displayed in Figs. 4(a) and 4(b) for monolayer BP with different initial wave vectors and for multilayer BP with the fixed value $k_0 = 0.1\,\text{Å}^{-1}$, respectively. By comparing Figs. 4(a) and 4(b) with Figs. 2(a) and 2(b), one can notice that the ZBW for the pseudospin $[1,1]^T$ exhibit a smaller (larger) oscillation frequency (period) than for the case $[1,0]^T$ [see insets in Figs. 4(a) and 4(b)], with the total average position $\langle y(t)\rangle$ moving faster along the positive y direction than for the case $[1,0]^T$ that moves along the negative y direction. This statement is confirmed by the time derivative $\langle v_y(t)\rangle = \frac{d\langle y(t)\rangle}{dt}$ of the results shown in Figs. 4(a) and 4(b), as demonstrated in Figs. 4(c) and 4(d), that converges to clearly nonzero and larger final values as compared to the ones obtained in Figs. 2(c) and 2(d). In general, the main features of the ZBW remain the same as the previous case: the dependence of the transient character, as well as the different amplitude, frequency and duration time of the ZBW for different initial wave vector and number of layers. For the expectation values of the velocities [Figs. 4(c) and 4(d)], note that in contrast to Figs. 2(c) and 2(d), in the current case, the larger k_0, it leads to large oscillation amplitudes of $\langle v_y(t)\rangle$. Moreover, the oscillatory behavior for multilayer BP [Figs. 4(b) and 4(d)] remains qualitatively the same as the one observed in Figs. 2(b) and 2(d) as compared to their monolayer BP results, except for the fact that in the $[1,1]^T$ case, the difference of the converging final values of $\langle v_y(t)\rangle$ are more pronounced for different numbers of layers.

In order to understand the origin of this weak oscillations and also the fast drift along the y direction for the pseudospin case $[1,1]^T$, we depict in Fig. 5 the spatial time evolution of the initial wave packet by showing snapshots for $t > 0$ of the total probability density. Note that the initial wave packet also splits into two parts propagating along y in opposite directions as in the $[1,0]^T$ case discussed in Sec. III A and shown in Fig. 3, but unlike the previous case, the portions of probability amplitudes and widths of the two subpackets are noticeably different, such that the electron probability density is not symmetric with respect to y at a fixed time step: $|\Psi(x,y,t)|^2 \neq |\Psi(x,-y,t)|^2$. This large asymmetry in

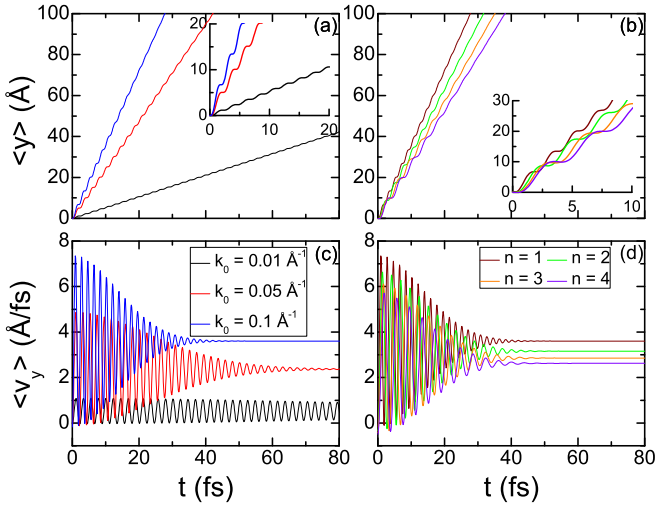

FIG. 4. The same as in Fig. 2, but now for the case $c_1 = 1$ and $c_2 = 1$.

the probability density explains the less evident ZBW effect in the average y position in Fig. 4, so that it becomes clear the reason why $\langle v_y(t)\rangle$ converges to nonzero values, which even increase with k_0, since a greater portion of the wave packet propagates to the positive y direction. Another feature of Fig. 5 is that the propagating wave packet does not deform as much as in the previous case, remaining approximately with the same packet width even after the splitting that originates a small subpacket moving in the opposite y direction.

C. $c_1 = 1$ and $c_2 = i$

The last investigated pseudospin polarization case is composed by the pseudospin components $c_1 = 1$ and $c_2 = i$. That means that all four BP sublattices are filled, but unlike the case $[1, 1]^T$ discussed in the previous Sec. III B, it has a phase difference between ϕ_1 and ϕ_2 that couples the pairs of subllatices A/D and B/C, respectively [see Eqs. (2) and (7)]. The reason for the study of this choice of pseudospin polarization is based on the corresponding interest in graphene case [43,54], since these two polarizations represent full-filled sublattice states points into perpendicular directions in monolayer graphene: $[1, 1]^T$ is directed along x axis at $t = 0$, whereas $[1, i]^T$ is directed along y axis at $t = 0$. From Eq. (14) for $c_1 = 1$ and $c_2 = i$, the wave function is given by

$$\Psi(\vec{r}, t) = \frac{1}{\sqrt{2}}\begin{pmatrix}\Phi_1(\vec{r}, t) + i\Phi_3(\vec{r}, t)\\ i\Phi_1(\vec{r}, t) + \Phi_2(\vec{r}, t)\end{pmatrix}. \tag{28}$$

Computing the average values for the position x and y using Eqs. (16) and (28), one obtains

$$\langle x(t)\rangle = -\frac{ie^{-a^2}}{\pi}\int_0^\infty\int_{-\pi}^{\pi} e^{-q^2+2aq\sin\beta}\left\{-\frac{i\chi^n\gamma_x^n\hbar^4d^2q^3\sin(2\beta)\sin(2\varepsilon_2(q,\beta)t/\hbar)\cos\theta_k(q,\beta)}{\left[\delta^n\hbar^2d^2+(\gamma_x^n\cos^2\beta+\gamma_y^n\sin^2\beta)q^2\hbar^2\right]^2+d^2(\chi^n)^2\hbar^4q^2\sin^2\beta}\right.$$
$$\left.+dq^2\cos\beta+\frac{2it\eta_x^nq^2\cos\beta}{\hbar d}+i\sin\theta_k(q,\beta)\left(\frac{2t\gamma_xq^2\cos\beta[\delta\hbar^2d^2+(\gamma_x\cos^2\beta+\gamma_y\sin^2\beta)q^2\hbar^2]}{\hbar^3d^3\varepsilon_2(q,\beta)}\right)\right\}d\beta dq, \tag{29a}$$

$$\langle y(t)\rangle = -\frac{ie^{-a^2}}{\pi}\int_0^\infty\int_{-\pi}^{\pi} e^{-q^2+2aq\sin\beta}\left\{\frac{iq\chi^n\hbar^2d^2\left[\delta^n\hbar^2d^2+\left(\gamma_x^n\cos^2\beta-\gamma_y^n\sin^2\beta\right)q^2\hbar^2\right]\sin(2\varepsilon_2(q,\beta)t/\hbar)\cos\theta_k(q,\beta)}{2\left[\delta^n\hbar^2d^2+(\gamma_x^n\cos^2\beta+\gamma_y^n\sin^2\beta)q^2\hbar^2\right]^2+2d^2(\chi^n)^2\hbar^4q^2\sin^2\beta}\right.$$
$$-adq+dq^2\sin\beta+\frac{2it\eta_y^nq^2\sin\beta}{\hbar d}-itq^2\sin\theta_k(q,\beta)$$
$$\left.\times\left(\frac{2\gamma_x^n\cos\beta[\delta^n\hbar^2d^2+(\gamma_x^n\cos^2\beta+\gamma_y^n\sin^2\beta)q^2\hbar^2]+(\chi^n)^2\hbar^2d^2\sin\beta}{\hbar^3d^3\varepsilon_2(q,\beta)}\right)\right\}d\beta dq. \tag{29b}$$

As in the previous cases, $\langle x(t)\rangle$ is unchanged with time due to initial configuration $k_0^x = 0$ in Eq. (13b). The results for $\langle y(t)\rangle$ and $\langle v_y(t)\rangle$ for different initial wave vectors and number of BP layers are shown in Figs. 6(a), 6(b) and 6(c), 6(d) respectively. As seen, these results also exhibit very pronounced ZBW and are more similar to the results shown in Fiqs. 2(a) and 2(b) for the case $[1, 0]^T$ concerning the large oscillation amplitudes, high oscillation frequency and small oscillation period, as compared to the ones shown in Fiqs. 4(a) and 4(b) for the $[1, 1]^T$ case. The reason for the pronounced ZBW effect in the cases $[1, 0]^T$ and $[1, i]^T$ can be linked to the unbalance and/or phase difference of the different pseudospin components. On the other hand, $\langle y(t)\rangle$ is shifted with time to positive y values, as in case $[1, 1]^T$ shown in Fiqs. 4(a) and 4(b), that suggests that the overall wave packet is propagating along the positive y direction. It is confirmed by the contour plots shown in Fig. 7 for the time evolution of the squared modulus of the wave function for different time steps. Similar to the previous cases, as the ZBW disappears, two separate parts of the initial wave packet are seen to move along the y axis with opposite velocities. Figure 7(d) shows that the two subpackets have different widths and thus the total wave-packet symmetry in y direction for a fixed time is not preserved, i.e., $|\Psi(x, y, t)|^2 \neq |\Psi(x, -y, t)|^2$, similar to the case $[1, 1]^T$. The dominant contribution to the total wave function is responsible for the positive shift in the average position $\langle y(t)\rangle$ and also for the nonzero values for the converging average velocities at large time steps.

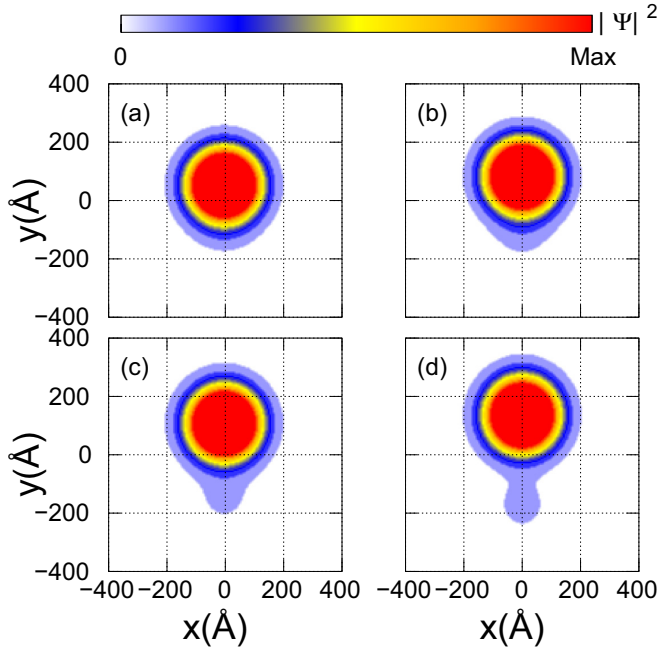

FIG. 5. The same as in Fig. 3, but now for the case $c_1 = 1$ and $c_2 = 1$.

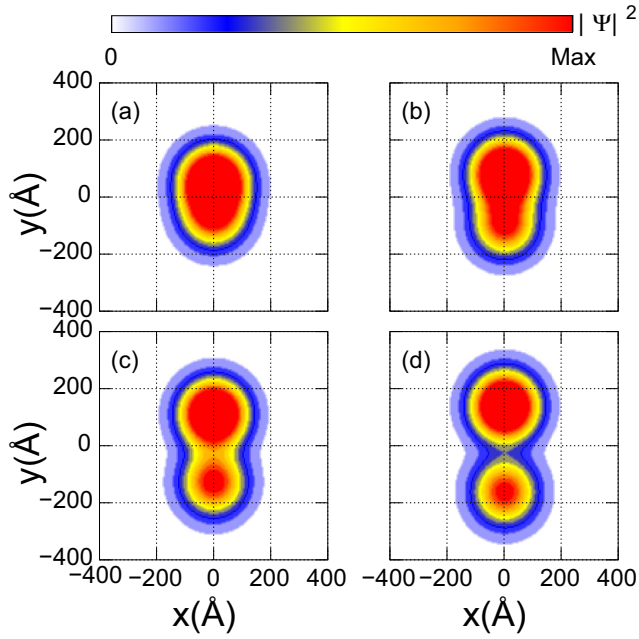

FIG. 7. The same as in Fig. 3, but now for the case $c_1 = 1$ and $c_2 = i$.

In order to check the agreement between the results obtained by using the two frameworks adopted here, namely, Green's function formalism (Sec. II B) and the split-operator technique (Sec. II C), we plot in Fig. 8 the comparison between them for two pseudospin configurations: [(a) and (b)] for the case $c_1 = 1$ and $c_2 = 1$ and [(c) and (d)] the case $c_1 = 1$ and $c_2 = i$. We have omitted such comparison for the case $c_1 = 1$ and $c_2 = 0$, since for the timescale, initial momentum values, and wave-packet width investigated in the current work, no difference at all was observed. It is really clear that both analytical (dashed curves) and numerical (solid curves) methods give similar qualitative results and illustrate similar ZBW. They have a good quantitative agreement, exhibiting a small discrepancy, for the worst case of ≈11% at maximum, as shown in the insets, and that occurs, in general, for much larger values of wave vector, and only after long time steps [see panels (a) and (b)], as well as fewer numbers of layers [see panels (c) and (d)]. The reason for such discrepancy for these two pseudopsin configuration must be related to inaccuracy in numerical integration to obtain the expectation

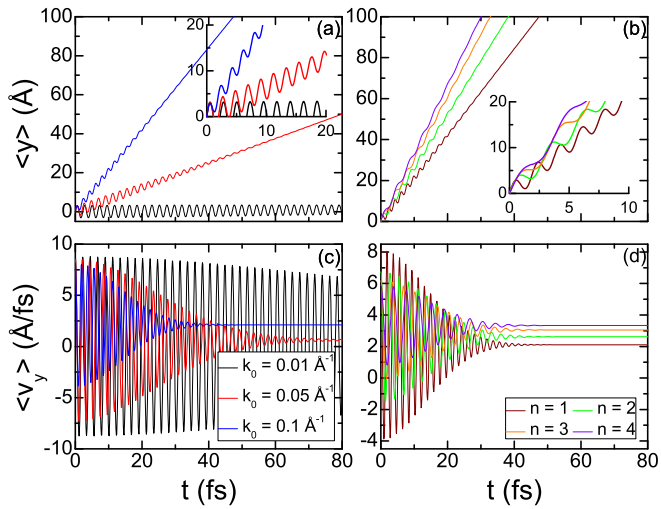

FIG. 6. The same as in Fig. 2, but now for the case $c_1 = 1$ and $c_2 = i$.

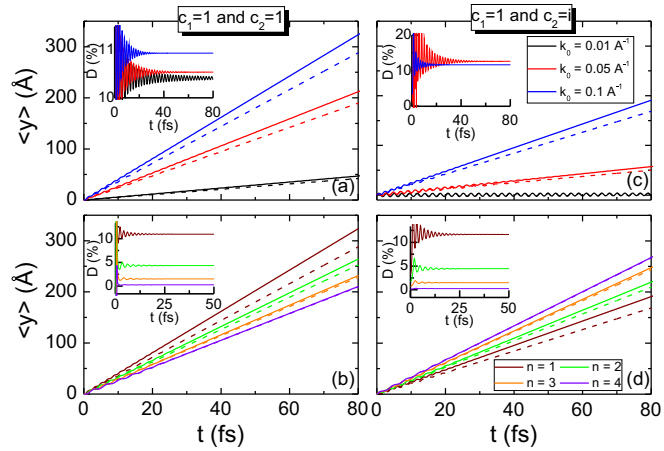

FIG. 8. Comparison between the results of the average position of a Gaussian wave packet of width $d = 100$ Å as a function of time obtained by (solid curves) the split-operator technique derived in Sec. II C and (dashed curves) analytical calculations derived in Sec. II B: [(a) and (b)] the case $c_1 = 1$ and $c_2 = 1$ and [(c) and (d)] the case $c_1 = 1$ and $c_2 = i$. [(a) and (c)] Wave packet propagating in a monolayer phosphorene sheet ($N = 1$) with different wave vectors: $k_0 = 0.01$ (black), 0.05 (red), and 0.1 Å^{-1} (blue). [(b) and (d)] Wave packet propagating in multilayer phosphorene ($N = 1, 2, 3, 4$) for fixed wave vector $k_0 = 0.1$ Å^{-1}.

values of the analytically derived position operators, since expressions (27a), (27b), (29a), and (29b) are more complicated as compared to the ones (25a) and (25b) for the case $[1, 0]^T$, in which both methods agree 100%, giving rise to these small deviations.

IV. VELOCITY OPERATOR

Let us now obtain the velocities along the x and y directions and verify whether v_x and v_y are constants of motion or not, which also indicates the directions where the ZBW manifests. To understand how this affects the velocity along certain directions, we use the Hamiltonian Eq. (1), or equivalently Eq. (3), for electrons in multilayer phosphorene, and calculate the commutators $[\mathcal{H}, v_x]$ and $[\mathcal{H}, v_y]$. According to the Heisenberg picture, the velocity operator is given by

$$\vec{v} = \frac{\partial \mathcal{H}}{\partial \vec{p}} = \frac{1}{\hbar}\frac{\partial \mathcal{H}}{\partial \vec{k}} = \frac{1}{i\hbar}[\vec{r}, \mathcal{H}], \tag{30}$$

with $\vec{v} = (v_x, v_y)$ and $\vec{r} = (x, y)$, yielding

$$v_x = \frac{2k_x}{\hbar}\left(\eta_x^n \mathbb{1} + \gamma_x^n \sigma_x\right), \tag{31a}$$

$$v_y = \frac{2k_y}{\hbar}\left(\eta_y^n \mathbb{1} + \gamma_y^n \sigma_x - \frac{\chi^n}{k_y}\sigma_z\right). \tag{31b}$$

Let us now verify whether v_x and v_y are constants of motion, and if there is any situation where v_x and v_y are not affected by the zitterbewegung. Evaluating $[\mathcal{H}, v_i]$ by making use of Eqs. (3) and (31), one obtains

$$[\mathcal{H}, v_x] = \frac{4i\epsilon_2}{\hbar} k_x \gamma_x^n \sin\theta_k \begin{pmatrix} -1 & 0 \\ 0 & 1 \end{pmatrix}, \tag{32a}$$

$$[\mathcal{H}, v_y] = \frac{4i\epsilon_2}{\hbar}\left[k_y \gamma_y^n \sin\theta_k + \chi^n \cos\theta_k\right]\begin{pmatrix} -1 & 0 \\ 0 & 1 \end{pmatrix}. \tag{32b}$$

Equation (32a) suggests that $[\mathcal{H}, v_x] = 0$ when

(i) $k_x = |k|\cos\beta = 0$ [that implies either $|k| = 0 \rightarrow k_x = k_y = 0$, i.e., zero initial momentum, or $\cos\beta = 0$ $(\sin\beta = \pm 1) \rightarrow \beta = \pm(2l+1)\pi/2$, with $l \in \mathbb{N}$];

(ii) $\sin\theta_k = 0 \rightarrow \theta_k = \pm l\pi$, with $l \in \mathbb{N}$ and consequently, by the definition of θ_k in Eq. (4c), one has $k_y = |k|\sin\beta = 0$ [that implies either $|k| = 0 \rightarrow k_x = k_y = 0$, i.e., zero initial momentum, or $\sin\beta = 0$ $(\cos\beta = \pm 1) \rightarrow \beta = \pm l\pi$, with $l \in \mathbb{N}$].

Thus v_x will be a constant of motion if $(k_x, k_y) = (0, \pm|k|)$ or $(k_x, k_y) = (\pm|k|, 0)$, corresponding to a constant motion along the y and x directions, respectively. On the other hand, $[\mathcal{H}, v_y]$ should be null if and only if k_y and $\cos\theta_k$ are both null, i.e., $\theta_k = \pm(2l+1)\pi/2$, with $l \in \mathbb{N}$. However, as mentioned in Sec. II A and shown in Figs. 1(c)–1(e), the phase angle of the pseudospin varies in the range $-\theta_k^{\max} \leqslant \theta_k \leqslant \theta_k^{\max}$, where $\theta_k^{\max}$ corresponds to the value of θ_k for $k_x = 0$ and $k_y = \pm 1$, being equivalent to $\beta = \pi/2$ [see Figs. 1(c)–1(e)]. Therefore one concludes that $[\mathcal{H}, v_y] \neq 0$, suggesting that: v_y is never a constant of motion, and the trembling motion along the y direction at small times for the wave-packet propagation in phosphorene systems is unavoidable, even for the case where one assumes $k_x = k_y = 0$, which yields

$$[\mathcal{H}, v_y]|_{k_x = k_y = 0} = \frac{4i\delta^n \chi^n}{\hbar}\begin{pmatrix} -1 & 0 \\ 0 & 1 \end{pmatrix}, \tag{33}$$

and, therefore, the wave packet will also move in the y direction. Similar behavior has been observed in previous works for graphene, where it was demonstrated both numerically [9,54] and analytically [43] within the Dirac and tight-binding models that even when $k_x = k_y = 0$ the wave-packet motion is still observed due to zitterbewegung effects. Considering the three different pseudospin configurations used here, one observes in Fig. 9 that this also holds for the electron motion in phosphorene for (black curve) $[c_1, c_2]^T = [1, 0]^T$ and (blue curve) $[c_1, c_2]^T = [1, i]^T$, exhibiting oscillations in the [Fig. 9(a)] average position and [Figs. 9(b) and 9(c)] velocity along y direction, similarly to the ones observed in Figs. 2 and 6 for small momentum values, but now with a much higher oscillation frequency and shorter period, that is clearly a consequence of the reduction of the momentum value. To understand the nature of such oscillations that counterintuitively appear even for the case with null initial momentum, we illustrate on the right panels of Fig. 9 the electron probability density (I) at $t = 390$ and (II) at 391 fs nearby a valley and a peak of the average velocity curve, corresponding to points with negative and positive velocities, respectively, as labeled in Fig. 9(c). It can be observed that the dispersion of the wave packet is just along the y direction, keeping its radius along x direction practically unchanged from the initial circularly symmetric shape, and thus, for longer times, it becomes distorted into an elliptical shape. One can see by comparing panels I and II that for positive and negative points of the average velocity curve, the wave packet oscillates along y, such that the symmetry of the probability density concerning this axis changes over time, i.e., $|\Psi(x, y, t)|^2 \neq |\Psi(x, -y, t)|^2$. In the right panel, we show the isosurfaces at these two time steps (orange and green curves represent the states I and II), in order to emphasize that in fact the wave packet shakes around $y = 0$ while distorting along y direction. On the other hand, for the case $[c_1, c_2]^T = [1, 1]^T$ (red curves in Fig. 9) with null initial momentum $|k| = 0$, both the position and velocity averages along both x and y directions remain unchanged over time, although the wave packet also distorts for this case along the y direction, exhibiting an elliptical shape for large time, but it deforms keeping the symmetry $|\Psi(x, y, t)|^2 = |\Psi(x, -y, t)|^2$.

V. CONCLUSIONS

In summary, we have studied the dynamics of free electrons described by an initial Gaussian wave packet in multilayer phosphorene samples by using the Green's function representation [21,43] and the continuum model [80] for low-energy electrons in N-layer BP. We performed analytical calculations to investigate the time evolution of some physical observables and, by regarding an arbitrary pseudospin amplitude for the BP sublattices, we obtained explicit analytical expressions for the two components of wave function and the expectation values of the x and y position operators. A numerical method based on the split-operator technique for N-layer BP system was also used, and its results were compared

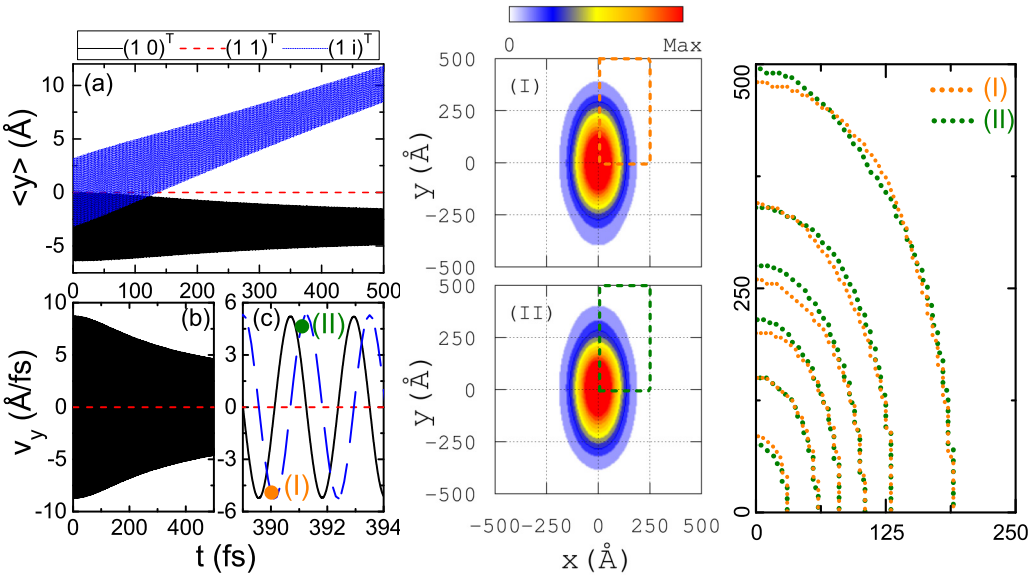

FIG. 9. (a) Average position and [(b) and (c)] expectation value of the velocity along y direction as a function of time for the case $[c_1, c_2]^T = [1, 0]^T$ (black), $[c_1, c_2]^T = [1, 1]^T$ (red), and $[c_1, c_2]^T = [1, i]^T$ (blue). (c) A magnification of the results in (b) for large time steps showing the oscillatory behavior of v_y. (Right) Contour plots of the squared modulus of the wave function at (I) $t = 390$ and (II) 391 fs, and a zoom emphasized by the dashed curves showing the isosurfaces at the two time steps.

to the analytical ones. Both analytical and numerical methods, reported here for the first time in the literature for N-layer phosphorene systems, illustrated similar effects, such as the packet splitting and ZBW oscillation, with a good qualitative and quantitative agreement. The methods exhibited a quantitative discrepancy for the worst case of $\approx 11\%$ at maximum and it occurs, in general, for very larger values of wave vector and after long time steps, as well as fewer numbers of layers, that it is related to two facts for (i) inaccuracy in numerical integration to obtain the expectation values of the analytically derived position operators and (ii) small numerical errors accumulated over the temporal evolution in split-operator technique.

The results obtained for infinite monolayer, bilayer, trilayer, and tetralayer phosphorene clearly demonstrate that the time evolution of wave function is accompanied by ZBW oscillations, which strongly depend on the initial pseudospin polarization, and decay of the wave-packet amplitude. The trembling motion and transient character of the ZBW were verified in the average position and average group velocity of the center mass of the propagated wave packet. The amplitude, frequency and duration time of the transient ZBW are shown to decay faster with increasing wave vector, due to wave-packet dispersion. It was also found that for the three investigated configurations of initial pseudospin, the oscillation amplitude of average position is more pronounced for the case $c_1 = 1$ and $c_2 = 0$, being related to the unbalance of the probability amplitude on the BP sublattices. Moreover, we showed that electrons moving in N-layer phosphorene exhibit qualitatively similar results as the ones observed in the monolayer BP case, except for the oscillation phase difference and final group velocity achieved after the transient behavior, that is caused by the different curvature of the energy bands for the different N-layer phosphorene, and consequently different effective masses and Hamiltonian parameters in the continuum model. In addition, the anisotropic character of the N-layer BP energy bands and their effective masses along the x and y directions imply an elliptical shape for the propagated wave packet, since the group velocity is also consequently anisotropic, i.e., it is greater in one direction than the other leading to a nonuniform propagation along the different directions. This elliptical shape for the propagated wave packet in N-layer BP is not observed in other isotropic materials, such as monolayer and bilayer graphene, whose group velocities are the same along both zigzag and armchair directions. This is related to the linear dependence on k_y in the out-of-diagonal terms in the BP Hamiltonian, that implies, for small momentum values, a Schrödinger-like (Dirac-like) behavior along the zigzag (armchair) direction for the electrons, bringing up very interesting consequences in the wave-packet dynamics in phosphorene systems.

In order to understand in more details, the nature of the transient character of the ZBW effect in multilayer BP systems, we investigated numerically also the spatial evolution of the initial wave packet by showing snapshots for $t > 0$ of the probability density of the wave function. We demonstrated the effect of the packet splitting is associated to the ZBW. This splitting of the wave packets in two parts appears due to the presence of the electron states with a Gaussian distribution of negative and positive momenta, which propagate with different group velocity in opposite directions. Furthermore, based on the Heisenberg picture and by the calculation of the velocity operators, we demonstrated that the trembling motion along the y direction at small times for the wave-packet propagation in phosphorene systems is unavoidable even for null initial momentum.

Although no experimental measurement about the ZBW effect in BP system has been reported in the literature up to

the date, we believe that the theoretical descriptions developed here for the time evolution of wave-packet propagation in multilayer BP systems will make possible further investigations of transport properties in a plenty of BP-based materials in the presence or absence of external fields.

ACKNOWLEDGMENTS

This work was financially supported by the Brazilian Council for Research (CNPq), under the PRONEX/FUNCAP and CAPES foundation. We thank Tony Low for helpful comments and fruitful discussions.

[1] W. Zawadzki and T. M. Rusin, Zitterbewegung (trembling motion) of electrons in semiconductors: A review, J. Phys.: Condens. Matter **23**, 143201 (2011).

[2] W. Zawadzki, Semirelativity in semiconductors: A review, J. Phys.: Condens. Matter **29**, 373004 (2017).

[3] E. Schrödinger, Über die kraftefreie bewegung in der relativistishen quantenmechanik, Sitzungsber. Preuss. Akad. Wiss. Phys. Math. Kl. **24**, 418 (1930).

[4] A. O. Barut and A. J. Bracken, Zitterbewegung and the internal geometry of the electron, Phys. Rev. D **23**, 2454 (1981).

[5] H. Feschbach and F. Villars, Elementary relativistic wave mechanics of spin 0 and spin 1/2 particles, Rev. Mod. Phys. **30**, 24 (1958).

[6] A. O. Barut and W. Thacker, Covariant generalization of the zitterbewegung of the electron and its SO(4, 2) and SO(3, 2) internal algebras, Phys. Rev. D **31**, 1386 (1985).

[7] K. Huang, On the zitterbewegung of the Dirac electron, Am. J. Phys. **20**, 479 (1952).

[8] J. A. Lock, The zitterbewegung of a free localized Dirac particle, Am. J. Phys. **47**, 797 (1979).

[9] B. Thaller, Visualizing the kinematics of relativistic wave packets, arXiv:quant-ph/0409079.

[10] J. W. Braun, Q. Su, and R. Grobe, Numerical approach to solve the time-dependent Dirac equation, Phys. Rev. A **59**, 604 (1999).

[11] F. Cannata, L. Ferrari, and G. Russo, Dirac-like behavior of a non-relativistic tight binding Hamiltonian in one dimension, Solid State Commun. **74**, 309 (1990).

[12] L. Ferrari and G. Russo, Nonrelativistic zitterbewegnng in two-band systems, Phys. Rev. B **42**, 7454 (1990).

[13] F. Cannata and L. Ferrari, Effects of the nonrelativistic zitterbemegung on the electron-phonon interaction in two-band systems, Phys. Rev. B **44**, 8599 (1991).

[14] D. Lurié and S. Cremer, Zitterbewegung of quasiparticles in superconductors, Physica (Amsterdam) **50**, 224 (1970).

[15] J. Cserti and G. Dávid, Unified description of zitterbewegung for spintronic, graphene, and superconducting systems, Phys. Rev. B **74**, 172305 (2006).

[16] J. Schliemann, D. Loss, and R. M. Westervelt, Zitterbewegung of Electronic Wave Packets in III-V Zinc-Blende Semiconductor Quantum Wells, Phys. Rev. Lett. **94**, 206801 (2005).

[17] J. Schliemann, D. Loss, and R. M. Westervelt, Zitterbewegung of electrons and holes in III-V semiconductor quantum wells, Phys. Rev. B **73**, 085323 (2006).

[18] S.-Q. Shen, Spin Transverse Force on Spin Current in an Electric Field, Phys. Rev. Lett. **95**, 187203 (2005).

[19] Z. F. Jiang, R. D. Li, S.-C. Zhang, and W. M. Liu, Semiclassical time evolution of the holes from Luttinger Hamiltonian, Phys. Rev. B **72**, 045201 (2005).

[20] P. Brusheim and H. Q. Xu, Spin Hall effect and zitterbewegung in an electron waveguide, Phys. Rev. B **74**, 205307 (2006).

[21] V. Y. Demikhovskii, G. M. Maksimova, and E. V. Frolova, Wave packet dynamics in a two-dimensional electron gas with spin orbit coupling: Splitting and zitterbewegung, Phys. Rev. B **78**, 115401 (2008).

[22] T. Biswas and T. K. Ghosh, Wave packet dynamics and zitterbewegung of heavy holes in a quantizing magnetic field, J. Appl. Phys. **115**, 213701 (2014).

[23] W. Zawadzki, Zitterbewegung and its effects on electrons in semiconductors, Phys. Rev. B **72**, 085217 (2005).

[24] X. Zhang, Observing Zitterbewegung for Photons Near the Dirac Point of a Two-Dimensional Photonic Crystal, Phys. Rev. Lett. **100**, 113903 (2008).

[25] F. Dreisow, M. Heinrich, R. Keil, A. Tünnermann, S. Nolte, S. Longhi, and A. Szameit, Classical Simulation of Relativistic Zitterbewegung in Photonic Lattices, Phys. Rev. Lett. **105**, 143902 (2010).

[26] X. Zhang and Z. Liu, Extremal Transmission and Beating Effect of Acoustic Waves in Two-Dimensional Sonic Crystals, Phys. Rev. Lett. **101**, 264303 (2008).

[27] R. Gerritsma, G. Kirchmair, F. Zähringer, E. Solano, R. Blatt, and C. F. Roos, Quantum simulation of the Dirac equation, Nature (London) **463**, 68 (2010).

[28] T. M. Rusin and W. Zawadzki, Zitterbewegung of relativistic electrons in a magnetic field and its simulation by trapped ions, Phys. Rev. D **82**, 125031 (2010).

[29] V. Y. Demikhovskii, G. M. Maksimova, and E. V. Frolova, Wave packet dynamics in hole Luttinger systems, Phys. Rev. B **81**, 115206 (2010).

[30] R. Winkler, U. Zulicke, and J. Bolte, Oscillatory multiband dynamics of free particles: The ubiquity of zitterbewegung effects, Phys. Rev. B **75**, 205314 (2007).

[31] J. Y. Vaishnav and C. W. Clark, Observing Zitterbewegung with Ultracold Atoms, Phys. Rev. Lett. **100**, 153002 (2008).

[32] Y. C. Zhang, S. W. Song, C. F. Liu, and W. M. Liu, Zitterbewegung effect in spin-orbit-coupled spin-1 ultracold atoms, Phys. Rev. A **87**, 023612 (2013).

[33] L. K. Shi, S. C. Zhang, and K. Chang, Anomalous electron trajectory in topological insulators, Phys. Rev. B **87**, 161115(R) (2013).

[34] L. K. Shi and K. Chang, Probing electron zitterbewegung in topological insulators, arXiv:1109.4771v4 (2011).

[35] L.-G. Wang, Z.-G. Wang, and S.-Y. Zhu, Zitterbewegung of optical pulses near the Dirac point inside a negative-zero-positive index metamaterial, Europhys. Lett. **86**, 47008 (2009).

[36] L. J. LeBlanc, M. C. Beeler, K. Jimenez-Garcia, A. R. Perry, S. Sugawa, R. A. Williams, and I. B. Spielman, Direct observation of zitterbewegung in a Bose-Einstein condensate, New J. Phys. **15**, 073011 (2013).

[37] C. Qu, C. Hamner, M. Gong, C. Zhang, and P. Engels, Observation of zitterbewegung in a spin-orbit-coupled Bose-Einstein condensate, Phys. Rev. A **88**, 021604(R) (2013).

[38] K. S. Novoselov, A. K. Geim, S. V. Morozov, D. Jiang, Y. Zhang, S. V. Dubonos, I. V. Grigorieva, and A. A. Firsov, Electric field effect in atomically thin carbon films, Science **306**, 666 (2004).

[39] K. S. Novoselov, A. K. Geim, S. V. Morozov, D. Jiang, M. I. Katsnelson, I. V. Grigorieva, S. V. Dubonos, and A. A. Firsov, Two-dimensional gas of massless Dirac fermions in graphene, Nature (London) **438**, 197 (2005).

[40] A. H. C. Neto, F. Guinea, N. M. R. Peres, K. S. Novoselov, and A. K. Geim, The electronic properties of graphene, Rev. Mod. Phys. **81**, 109 (2009).

[41] M. I. Katsnelson, *Graphene: Carbon in Two Dimensions* (Cambridge University Press, Cambridge, 2012).

[42] M. I. Katsnelson, Zitterbewegung, chirality, and minimal conductivity in graphene, Eur. Phys. J. B **51**, 157 (2006).

[43] G. M. Maksimova, V. Y. Demikhovskii, and E. V. Frolova, Wave packet dynamics in a monolayer graphene, Phys. Rev. B **78**, 235321 (2008).

[44] J. C. Martinez, M. B. A. Jalil, and S. G. Tan Martinez, Klein tunneling and zitterbewegung and the formation of a polarized p-n junction in graphene, Appl. Phys. Lett. **97**, 062111 (2010).

[45] R. Englman and T. Vértesi, Large Berry phases in layered graphene, Phys. Rev. B **78**, 205311 (2008).

[46] T. M. Rusin and W. Zawadzki, Transient zitterbewegung of charge carriers in mono-and bilayer graphene, and carbon nanotubes, Phys. Rev. B **76**, 195439 (2007).

[47] T. M. Rusin and W. Zawadzki, Theory of electron zitterbewegung in graphene probed by femtosecond laser pulses, Phys. Rev. B **80**, 045416 (2009).

[48] T. M. Rusin and W. Zawadzki, Zitterbewegung of electrons in graphene in a magnetic field, Phys. Rev. B **78**, 125419 (2008).

[49] W. Zawadzki and T. M. Rusin, Zitterbewegung (trembling motion) of electrons in narrow-gap semiconductors, J. Phys.: Condens. Matter **20**, 454208 (2008).

[50] V. Krueckl and T. Kramer, Revivals of quantum wave packets in graphene, New J. Phys. **11**, 093010 (2009).

[51] E. Romera and F. de los Santos, Revivals, classical periodicity, and zitterbewegung of electron currents in monolayer graphene, Phys. Rev. B **80**, 165416 (2009).

[52] J. Schliemann, Cyclotron motion in graphene, New J. Phys. **10**, 043024 (2008).

[53] Y. X. Wang, Z. Yang, and S. J. Xiong, Study of zitterbewegung in graphene bilayer with perpendicular magnetic field, Europhys. Lett. **89**, 17007 (2010).

[54] A. Chaves, L. Covaci, Kh. Yu. Rakhimov, G. A. Farias, and F. M. Peeters, Wave-packet dynamics and valley filter in strained graphene, Phys. Rev. B **82**, 205430 (2010).

[55] L. Li, Y. Yu, G. J. Ye, Q. Ge, X. Ou, H. Wu, D. Feng, X. H. Chen, and Y. Zhang, Black phosphorus field-effect transistors, Nat. Nanotechnol. **9**, 372 (2014).

[56] H. Liu, A. T. Neal, Z. Zhu, Z. Luo, X. Xu, D. Tománek, and P. D. Ye, Phosphorene: An unexplored 2D semiconductor with a high hole mobility, ACS Nano **8**, 4033 (2014).

[57] F. Xia, H. Wang, and Y. Jia, Rediscovering black phosphorus as an anisotropic layered material for optoelectronics and electronics, Nat. Commun. **5**, 4458 (2014).

[58] S. P. Koenig, R. A. Doganov, H. Schmidt, A. H. Castro Neto, and B. Özyilmaz, Electric field effect in ultrathin black phosphorus, Appl. Phys. Lett. **104**, 103106 (2014).

[59] A. Castellanos-Gomez, L. Vicarelli, E. Prada, J. O. Island, K. L. Narasimha-Acharya, S. I. Blanter, D. J. Groenendijk, M. Buscema, G. A. Steele, J. V. Alvarez, H. W. Zandbergen, J. J. Palacios, and H. S. J. van der Zant, Isolation and characterization of few-layer black phosphorus, 2D Mater. **1**, 025001 (2014).

[60] P. Avouris, T. F. Heinz, and T. Low, *2D Materials* (Cambridge University Press, 2017).

[61] A. S. Rodin, A. Carvalho, and A. H. Castro Neto, Strain-Induced Gap Modification in Black Phosphorus, Phys. Rev. Lett. **112**, 176801 (2014).

[62] V. Tran, R. Soklaski, Y. Liang, and L. Yang, Layer-controlled band gap and anisotropic excitons in few-layer black phosphorus, Phys. Rev. B **89**, 235319 (2014).

[63] A. Castellanos-Gomez, Black phosphorus: Narrow gap, wide applications, J. Phys. Chem. Lett. **6**, 4280 (2015).

[64] K. Dolui and S. Y. Quek, Quantum-confinement and structural anisotropy result in electrically-tunable dirac cone in few-layer black phosphorous, Sci. Rep. **5**, 11699 (2015).

[65] S. Das, W. Zhang, M. Demarteau, A. Hoffmann, M. Dubey, and A. Roelofs, Tunable transport gap in phosphorene, Nano Lett. **14**, 5733 (2014).

[66] J. Kim, S. S. Baik, S. H. Ryu, Y. Sohn, S. Park, B.-G. Park, J. Denlinger, Y. Yi, H. J. Choi, and K. S. Kim, Observation of tunable band gap and anisotropic Dirac semimetal state in black phosphorus, Science **349**, 723 (2015).

[67] S. Yuan, E. van Veen, M. I. Katsnelson, and R. Roldán, Quantum Hall effect and semiconductor-to-semimetal transition in biased black phosphorus, Phys. Rev. B **93**, 245433 (2016).

[68] G. Zhang, S. Huang, A. Chaves, C. Song, V. O. Özçelik, T. Low, and H. Yan, Infrared fingerprints of few-layer black phosphorus, Nat. Commun. **8**, 14071 (2017).

[69] D. J. P. de Sousa, L. V. de Castro, D. R. da Costa, J. M. Pereira, and T. Low, Multilayered black phosphorus: From a tight-binding to a continuum description, Phys. Rev. B **96**, 155427 (2017).

[70] T. Low, A. S. Rodin, A. Carvalho, Y. Jiang, H. Wang, F. Xia, and A. C. Neto, Tunable optical properties of multilayer black phosphorus thin films, Phys. Rev. B **90**, 075434 (2014).

[71] T. Low, R. Roldán, H. Wang, F. Xia, P. Avouris, L. M. Moreno, and F. Guinea, Plasmons and Screening in Monolayer and Multilayer Black Phosphorus, Phys. Rev. Lett. **113**, 106802 (2014).

[72] H. Yuan, X. Liu, F. Afshinmanesh, W. Li, G. Xu, J. Sun, B. Lian, A. G. Curto, G. Ye, Y. Hikita, Z. Shen, S.-C. Zhang, X. Chen, M. Brongersma, H. Y. Hwang, and Y. Cui, Polarization-sensitive broadband photodetector using a black phosphorus vertical p-n junction, Nat. Nanotechnol. **10**, 707 (2015).

[73] Q. Liu, X. Zhang, L. B. Abdalla, A. Fazzio, and A. Zunger, Switching a normal insulator into a topological insulator via electric field with application to phosphorene, Nano Lett. **15**, 1222 (2015).

[74] T. Low, M. Engel, M. Steiner, and P. Avouris, Origin of photoresponse in black phosphorus phototransistors, Phys. Rev. B **90**, 081408(R) (2014).

[75] R. Peng, K. Khaliji, N. Youngblood, R. Grassi, T. Low, and M. Li, Midinfrared electro-optic modulation in few-layer black phosphorus, Nano Lett. **17**, 6315 (2017).

[76] K. Khaliji, A. Fallahi, L. Martin-Moreno, and T. Low, Tunable plasmon-enhanced birefringence in ribbon array of anisotropic two-dimensional materials, Phys. Rev. B. **95**, 201401(R) (2017).

[77] E. Romera, J. B. Roldán, and F. de los Santos, Zitterbewegung in monolayer silicene in a magnetic field, Phys. Lett. A **378**, 2582 (2014).

[78] A. Singh, T. Biswas, T. K. Ghosh, and A. Agarwal, Wave packet dynamics in monolayer M_oS_2 with and without a magnetic field, Eur. Phys. J. B **87**, 275 (2014).

[79] J. M. Pereira and M. I. Katsnelson, Landau levels of single-layer and bilayer phosphorene, Phys. Rev. B **92**, 075437 (2015).

[80] D. J. P. de Sousa, L. V. de Castro, D. R. da Costa, and J. M. Pereira, Boundary conditions for phosphorene nanoribbons in the continuum approach, Phys. Rev. B **94**, 235415 (2016).

[81] A. Chaves, G. A. Farias, F. M. Peeters, and R. Ferreira, The split-operator technique for the study of spinorial wavepacket dynamics, Commun. Comput. Phys. **17**, 850 (2015).

[82] Kh. Yu. Rakhimov, A. Chaves, G. A. Farias, and F. M. Peeters, Wavepacket scattering of Dirac and Schrödinger particles on potential and magnetic barriers, J. Phys.: Condens. Matter **23**, 275801 (2011).

[83] J. M. Pereira, Jr., F. M. Peeters, A. Chaves, and G. A. Farias, Klein tunneling in single and multiple barriers in graphene, Semicond. Sci. Technol. **25**, 033002 (2010).

[84] M. H. Degani and M. Z. Maialle, Numerical calculations of the quantum states in semiconductor nanostructures, J. Comput. Theor. Nanosci. **7**, 454 (2010).

[85] A. A. Sousa, A. Chaves, T. A. S. Pereira, G. A. Farias, and F. M. Peeters, Quantum tunneling between bent semiconductor nanowires, J. Appl. Phys. **118**, 174301 (2015).

[86] A. Chaves, G. A. Farias, F. M. Peeters, and B. Szafran, Wave packet dynamics in semiconductor quantum rings of finite width, Phys. Rev. B **80**, 125331 (2009).

[87] M. D. Petrović, F. M. Peeters, A. Chaves, and G. A. Farias, Conductance maps of quantum rings due to a local potential perturbation, J. Phys.: Condens. Matter **25**, 495301 (2013).

[88] A. A. Sousa, A. Chaves, G. A. Farias, and F. M. Peeters, Braess paradox at the mesoscopic scale, Phys. Rev. B **88**, 245417 (2013).

[89] D. R. da Costa, A. Chaves, S. H. R. Sena, G. A. Farias, and F. M. Peeters, Valley filtering using electrostatic potentials in bilayer graphene, Phys. Rev. B **92**, 045417 (2015).

[90] D. R. da Costa, A. Chaves, G. A. Farias, L. Covaci, and F. M. Peeters, Wave-packet scattering on graphene edges in the presence of a pseudomagnetic field, Phys. Rev. B **86**, 115434 (2012).

[91] L. S. Cavalcante, A. Chaves, D. R. da Costa, G. A. Farias, and F. M. Peeters, All-strain based valley filter in graphene nanoribbons using snake states, Phys. Rev. B **94**, 075432 (2016).

[92] A. Chaves, D. R. da Costa, G. O. de Sousa, J. M. Pereira, Jr., and G. A. Farias, Energy shift and conduction-to-valence band transition mediated by a time-dependent potential barrier in graphene, Phys. Rev. B **92**, 125441 (2015).

[93] D. R. da Costa, A. Chaves, G. A. Farias, and F. M. Peeters, Valley filtering in graphene due to substrate-induced mass potential, J. Phys.: Condens. Matter **29**, 215502 (2017).

[94] A. N. Rudenko, S. Yuan, and M. I. Katsnelson, Toward a realistic description of multilayer black phosphorus: From GW approximation to large-scale tight-binding simulations, Phys. Rev. B **92**, 085419 (2015).

[95] M. Massicotte, P. Schmidt, F. Vialla, K. G. Schädler, A. Reserbat-Plantey, K. Watanabe, T. Taniguchi, K. J. Tielrooij, and F. H. L. Koppens, Picosecond photoresponse in van der Waals heterostructures, Nat. Nanotech. **11**, 42 (2016).

[96] T. M. Rusin and W. Zawadzki, Zitterbewegung of electrons in carbon nanotubes created by laser pulses, J. Phys.: Condens. Matter **26**, 215301 (2014).